The role of microscopic displacement dynamics for underground hydrogen versus natural gas storage in fractured reservoirs

Sojwal Manoorkar[a,b,*], Gülce Kalyoncu Pakkaner[a,b], Hamdi Omar[a,b], Soetkin Barbaix[a,b], Dominique Ceursters[c], Maxime Latinis[c], Stefanie Van Offenwert[c], Tom Bultreys[a,b]

[a]*Department of Geology, Ghent University, Ghent, Belgium*
[b]*Centre for X-ray Tomography (UGCT), Ghent University, Ghent, Belgium*
[c]*Fluxys, Belgium*

Abstract

Repurposing natural gas (methane) storage facilities to hydrogen storage leverages existing infrastructure to address seasonal energy demand-supply fluctuations. However, the differences in the injection-withdrawal cycle between hydrogen and methane-brine systems remain poorly understood. Therefore, we investigate the pore-scale two-phase flow dynamics of hydrogen (H_2), methane (CH_4), and their mixtures (50% H_2-50% CH_4, 95% H_2-5% CH_4) in fractured limestone from the Loenhout natural gas storage aquifer in Belgium. The controlled single-cycle primary drainage and imbibition experiments were conducted at 10 MPa and 65°C, typical reservoir conditions for three different rock samples. Our results show that H_2, CH_4, and their mixtures exhibit similar average gas saturations after drainage, though invasion patterns depend on fracture geometry. Rougher fractures

---

[*]I am corresponding author
Email address: `sojwal.manoorkar@Ugent.be/sojwal.m@gmail.com` (Sojwal Manoorkar)

exhibit discontinuous invasion, dominated by roof snap-off events, with H_2 forming a greater number of smaller ganglia compared to CH_4, likely due to hydrogen's lower viscosity. Fractured rock with a wider aperture achieves higher gas saturation during drainage but shows lower recovery efficiency due to increased residual trapping. During imbibition, gas type plays a more significant role, unlike drainage. In a pore-scale sample (D = 6 mm), hydrogen achieves 100% recovery in smoother, narrower fractures, whereas methane and its mixtures experience notable trapping. In rougher fractures, both gases are retained, but H_2 forms fewer, more connected clusters, while CH_4 forms smaller, fragmented ganglia, influencing storage capacity, leakage risk, and recovery efficiency. These findings highlight uncertainties in current methodologies for cyclical operations in underground hydrogen storage and emphasize the need for improved predictive models.

1. Introduction

The transition to a zero-carbon energy economy is increasingly recognized to be essential for mitigating climate change, with hydrogen emerging as a key component in this transformation [1, 2, 3]. Effective hydrogen storage solutions are required to meet the projected demand of several Giga-tons globally for a sustainable energy future. Underground hydrogen storage (UHS) in porous geological formations presents a viable strategy, enabling the storage of excess electricity in the form of hydrogen in subsurface environments, such as saline aquifers and depleted gas fields. This approach

has similarities to the storage of CO_2 in saline aquifers, offering large storage capacities [1, 4, 3, 5, 6]. However, unlike CO_2, hydrogen storage necessitates seasonal withdrawal to meet fluctuating electricity demands. A rapid and cost effective strategy could involve converting existing underground natural gas storage (UNGS) facilities and depleted oil and gas reservoirs to hydrogen storage, capitalizing on established infrastructure and technical expertise [7, 8].

A notable candidate for such conversion is the Loenhout facility in northern Belgium, where methane is currently stored in fractured karstic limestone of the Visean age, characterized by low matrix permeability. Flow in this reservoir predominantly occurs through a fracture network, a feature common to many reservoirs, whether naturally formed or induced during injection operations. Furthermore, hydrogen's low density and high diffusivity increase the risk of leakage through faults and fractures in the sealing caprock [9, 10], highlighting the importance of understanding fracture flow dynamics for effective gas storage. Converting natural gas storage sites to hydrogen storage necessitates a detailed investigation of the differences in flow dynamics between methane-brine and hydrogen-brine systems. To determine the economic feasibility of such a conversion and to optimize storage operations, it is essential to study the pore-scale mechanisms governing gas displacement within the reservoir rock. Understanding displacement dynamics, as addressed in this study, is a prerequisite for analyzing relative permeability, which is presented in a submitted companion paper [11]. These investigations provide critical insights into flow, transport, and trapping behaviors [12, 13, 14].

Two-phase displacement dynamics are mainly governed by the balance between nonlocal viscous forces and local capillary pressures acting on fluid menisci. The relative influence of these forces is captured by dimensionless numbers, such as the capillary number ($Ca = \frac{\mu_i u_i}{\sigma}$) and the viscosity ratio ($M = \frac{\mu_i}{\mu_d}$), where μ_i and μ_d are the viscosities of the invading and defending fluids, u_i is the Darcy velocity of the invading fluid, and σ is the interfacial tension. In fractured media, these forces are influenced by both fluid properties and fracture geometry, characterised by varying aperture and surface roughness. Such geometrical heterogeneity intensifies phase interference, where the presence of one fluid affects the displacement efficiency of the other [15, 16, 17]. The invasion patterns resulting from higher phase interference during hydrogen-brine flow in rough fractures remain poorly understood, highlighting a significant knowledge gap. Hydrogen's very low viscosity and density result in flow behaviors that are distinct from other gases, with significantly different effective permeability, as explored in recent porous media studies [18, 19, 20, 21, 12, 14, 22, 13]. These differences emphasize the need for dedicated investigations into hydrogen-brine flow in fractured systems.

Several studies have visualized and quantified displacement dynamics in fractures using both transparent models [23] and natural rocks [24, 25, 26]. Advanced XCT and fast synchrotron imaging have been employed by Phillips et al. [27, 28] to investigate the influence of fracture roughness on displacement processes. However, most existing studies focus on oil-water or air-water systems, which fail to capture hydrogen's unique characteristics. Early foundational work by Fourar et al. [29], Fourar [30] on air-water flow in narrow, smooth, and rough fractures demonstrated that flow patterns in frac-

tures are significantly different from those in porous media, making conventional porous media models unsuitable for hydrogen flow in fractures. These findings have been supported by numerical studies, including continuum-based flow models [31], pore-network models representing fracture voids [32, 24], and lattice-Boltzmann methods [33]. However, these methods remain unverified for hydrogen-brine flow, and conclusions drawn from porous media studies cannot be directly extrapolated to fractured systems. Understanding hydrogen-brine invasion patterns through fractured media is crucial, as they directly influence upscaled properties like relative permeability and trapping [24, 25, 26, 34, 35]. Understanding hydrogen-brine invasion patterns in fractured media is critical, as they directly govern upscaled properties such as relative permeability and trapping [24, 25, 26, 34, 35]. Addressing this knowledge gap will advance the development of models for hydrogen flow and storage in fractured reservoirs.

Motivated by the goal of converting existing gas storage facilities in fractured aquifers to hydrogen storage, we systematically investigated hydrogen-brine and methane-brine displacement dynamics across various fracture geometries under subsurface-relevant capillary numbers during both drainage and imbibition. The experiments included H_2, CH_4, and H_2-CH_4 mixtures, as methane is present in the current natural gas storage reservoir at Loenhout site and can act as a cushion gas for new potential sites, making the behavior of mixtures crucial to study. Using X-ray computed tomography (XCT) imaging, we visualized microscopic-scale fluid distributions after the displacement processes, identifying preferential fluid pathways, saturation levels, and residual trapping within fractures. These pore-scale observations

are critical for refining upscaled capillary pressure and relative permeability models, contributing to improved predictions of multiphase flow behavior in fractured systems.

2. Materials and methods

2.1. Rocks and fluids

Carbonate mudstone samples from wells DZH 24 and DZH 26 of the underground storage facility at Loenhout, Belgium, were obtained for this study. These rocks belong to the Loenhout Formation, part of the Carboniferous Limestone Group in the Campine-Brabant Basin (Northern Belgium). The samples are limestones of Viséan (Dinantian) age [36, 37, 38]. The rock matrix exhibits porosity values of less than 0.01 and permeability below 1 mD, indicating that fluid flow in the field is predominantly controlled by the fracture network. For this study, three cylindrical samples with varying diameters and lengths were drilled from larger cores. Experiment 1 was performed on sample which had a diameter of 6 mm and a length of 22 mm. Experiments 2 and 3 were conducted on samples, both having a diameter of 25 mm and a length of 45 mm. All samples were fractured using the Brazilian tensile stress test, sample 1 with a miniature compression stage (Deben CT5000, UK) and samples 2 and 3 at Laboratorium Magnel for Concrete study at Ghent University. In Experiment 3, the fracture was further widened by embedding approximately 8 -10 glass beads of 500 µm, which were randomly distributed within the fracture as propants to obtain a wider fracture aperture. A summary of the different samples used in this study is provided in Table 1.

Table 1: Sample and fracture sizes of different cores

Exp	well	Diameter mm	Length mm	aperture µm	Porosity	Permeability D
1	DZH 24	6	22	130	0.011	38
2	DZH 24	25	45	255	0.008	79
3	DZH 26	25	45	450	0.009	298

Table 2: Thermophysical properties of fluids at temperature 338 K and pressure 10 MPa

Fluid	Density kg m^{-3}	Viscosity Pa.s x 10^{-6}	Interfacial tension mN $\cdot$ m^{-1}
H_2	7	9.8	70
CH_4	61	14.4	50
H_2-CH_4 (95:5)	9.7	10	69
H_2-CH_4 (50:50)	34	1.21	60
20 wt% KI	1800	980	72
25 wt% KI	2080	915	72

99.999% pure H_2 and CH_4 (supplied by AirLiquide) are used as the non-wetting phase. The gas mixture is prepared based on partial pressure. For the wetting phase, brine is prepared using potassium iodide, KI (Sigma-Aldrich) and deionized water. In Exp 1, a 20 wt% KI brine is used, while a 25 wt% KI brine is used for Exp 2 and 3. The concentration of the brine is determined based on the required X-ray contrast between brine and gas in the micro-CT scans performed in the experiments. The fluid properties are summarized in Table 2.

2.2. Experimental setup and procedure

The core-flooding experiments were conducted under a capillary-dominant flow regime using unsteady-state drainage and imbibition. The capillary

Table 3: Experimental parameters used in this study. q is volumetric flow rate given in ml min^{-1} and Ca is the capillary number.

Exp no.	Gas	Drainage		Imbibition	
		q	Ca x 10^{-8}	q	Ca x 10^{-5}
Exp 1	H$_2$	0.1	30.5	0.05	1.43
	H$_2$ - CH$_4$ (50:50)	0.1	4.4	0.05	1.66
	CH$_4$	0.1	6.28	0.05	2.0
Exp 2	H$_2$	0.1	0.37	0.1	0.34
	H$_2$ - CH$_4$ (95:5)	0.096	0.37	0.096	0.46
	CH$_4$	0.048	0.37	0.049	0.17
Exp 3	H$_2$	0.39	0.8	0.1	0.19
	H$_2$ - CH$_4$(50:50)	0.16	0.48	0.1	0.22
	CH$_4$	0.11	0.47	0.1	0.27

number (Ca) was calculated as $Ca = \frac{\mu u}{\sigma}$, where μ represents the viscosity of the displacing fluid, σ denotes the interfacial tension, and u signifies the Darcy velocity of the injected (displacing) fluid. Three sets of experiments were performed with varying sample and fracture sizes, as explained in section 2.1 . The calculated capillary numbers for all the experiments conducted in this study are summarized in Table 3. The capillary number and viscosity ratio are overlaid on a phase diagram for porous media [39] as shown in Figure S1 in Supplementary Information S1, indicating that the displacement dynamics is expected to be capillary fingering.

The experimental setup is shown in Figure 1. The sample is mounted in an X-ray transparent flow cell (RS system, Norway), with stainless steel tubing employed to inject fluids through the fractured sample. Heating tape was wrapped around the core holder to maintain the core at 65°C. A stirred reactor (Parr Instruments) is used to pre-equilibrate the brine and gas at 100 bar pressure and a temperature of 65°C. A high pressure reciprocal pump

(Teledyne ISCO Reaxus, USA) was used to impose a confining pressure of 11.5 MPa on the sleeve around the sample. A high pressure syringe pump (Vindum Engineering VP12K) was deployed to saturate and pressurize the sample with brine. Another syringe pump (ISCO 500D) was utilized to pull pre-equilibrated gas or brine through the sample from the reactor. A pressure transducer (Keller PD-33X) was used to measure the differential pressure across the sample. To ensure safety when handling the flammable gases H_2 and CH_4, the reactor and ISCO pump were placed inside a low-oxygen cabinet to prevent the risk of fire.

The fractured limestone samples were vacuum-dried, wrapped with teflon tape and Aluminium foil to prevent gas leakage, and loaded into a Viton-sleeved core holder. A confining pressure of 15 bar was applied, and the setup was mounted vertically on an X-ray CT scanner for imaging. Absolute permeability was determined using Darcy's law, while fracture permeability was calculated via the local cubic law given by Equation 1, yielding values of 38 mD, 79 mD, and 298 mD for Experiments 1, 2, and 3, respectively. The samples were fully saturated with KI brine, heated to 65°C, and pressurized to 100 bar fracture pressure. Gas drainage and imbibition were conducted with equilibrated brine and gas (flow rates are mentioned in Table 3), and high-resolution scans were performed after each process. For Experiments 1 and 2, fluids were injected from the bottom, while Experiment 3 used top injection. Detailed procedures are provided in the Supplementary Information S2.

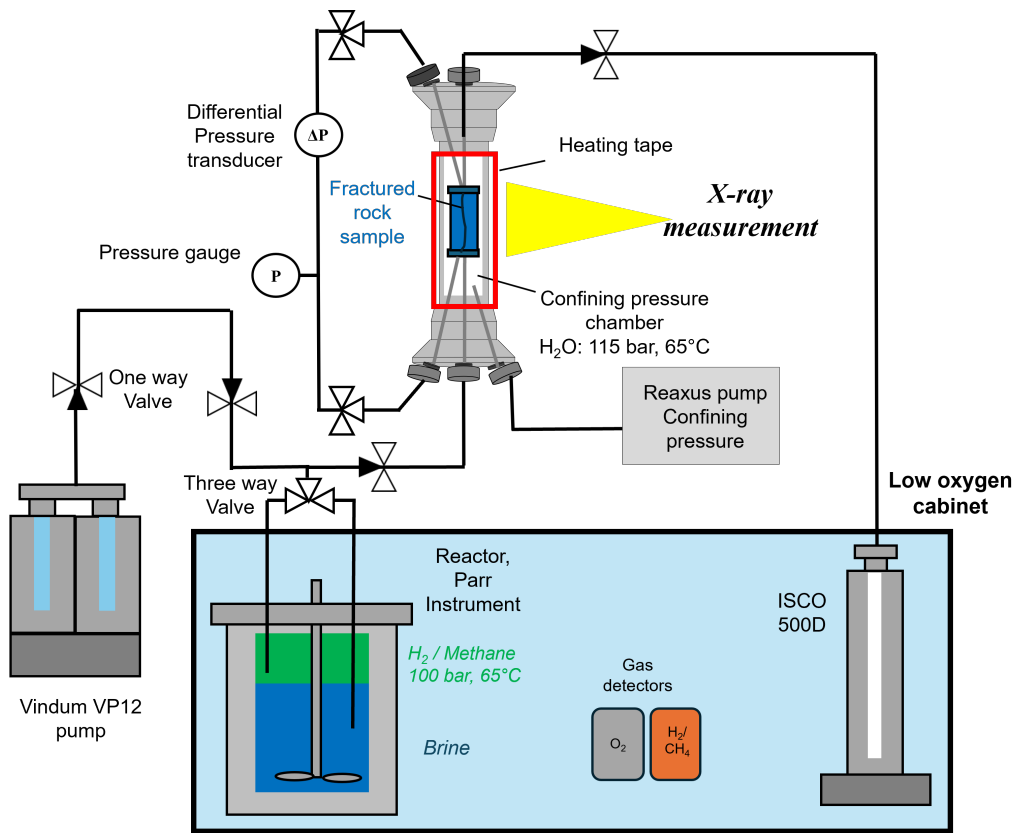$$Q = -\frac{D<b>^3}{12\mu}\frac{dP}{L} \tag{1}$$

Figure 1: Experimental set-up for two-phase hydrogen/methane-brine experiment performed with X-ray micro computed tomography scanner.

Table 4: Scanning parameters

Exp	Sample Dia (mm)	Scanner	Voltage (kV)	Exposure Time (ms)	Resolution (µm)	Projections
1	6	EMCT	90	120	6.57	2001
2	25	HECTOR	160	1000	20	2301
3	25	HECTOR	160	1000	20	2301

2.3. Imaging

X-ray imaging was performed during both the drainage and imbibition processes, using different scanners for the respective experiments.For Exp 1, imaging was performed using the Environmental Micro-CT (EMCT) scanner at the Center for X-ray Tomography (UGCT), Ghent University [40]. For Exp 2 and Exp 3, the High Energy CT Optimized for Research (HECTOR) scanner [41] at UGCT was employed, as it accommodates larger sample sizes. The scan parameters are summarized in Table 4.

The reconstructed images were processed using Avizo (ThermoFisher Scientific) software. First, all the images from the wet/fractional flow scans were registered to the dry scan using normalized mutual information, ensuring proper alignment. To enhance the signal-to-noise ratio, the scans were denoised using a non-local means filter. For segmentation, the fracture in the dry scan was identified using global thresholding, and this segmented fracture was then used as a mask to segment the flooding experiment scans. Within these masked images from the flooding experiments, the two phases (brine and gas) were segmented based on the histogram of the masked regions. The total porosity of the fracture was calculated from the volume fraction of the segmented dry scan. Aperture was obtained from the seg-

mented dry scan using the 'PoreSpy' Python toolkit [42], which calculates local thickness using maximal sphere approach. These processing steps allowed for a detailed quantification of fracture structure and fluid distribution during the experiments.

2.4. Saturation, curvature and contact angle

Quantitative analysis was conducted on the segmented wet scans to calculate gas saturation within the fracture during both drainage and imbibition. The wettability was determined based on Exp 1, due to the higher resolution of 6.57 μm. The gas-brine-rock contact angle was evaluated for drainage and imbibition on each voxel at the three-phase contact line. This was performed within a subvolume of 500 x 500 x 1170 voxels using an automated algorithm [43]. This method has been widely applied in previous studies, showing reasonable accuracy in contact angle measurement [44, 45, 12]. However, applying this algorithm at the current image resolution may introduce errors related to voxel size, as finer-scale features may not be fully captured. This could affect the precision of contact angle measurements at the three-phase contact line.

2.5. Fracture characterization

The experiments were conducted on fractured rock cores (Figure 2a), with average apertures of 130, 255, and 450 µm for Exp 1, 2, and 3 (Figure 2b). While roughness is assessed using the relative roughness index $\lambda_b = \frac{<b>^{\sigma}}{<b>_m}$ [46, 25, 47, 48, 28], we found it insufficient to capture the complexity of branching fracture networks. Greater roughness was qualitatively attributed

12

based on dry scan observations, as standard metrics failed to account for these features (details in Supplementary Information S3).

Figure 2c illustrates the 1-D porosity distribution along the sample lengths. Notably, the average porosity remains largely homogeneous across all three samples. However, despite similar average porosities, the fracture networks differ significantly: Sample 2 exhibits a network of numerous smaller fractures branching from the main fracture, Sample 3 features a single primary fracture along the length of the core and Sample 1 includes a horizontal branch.
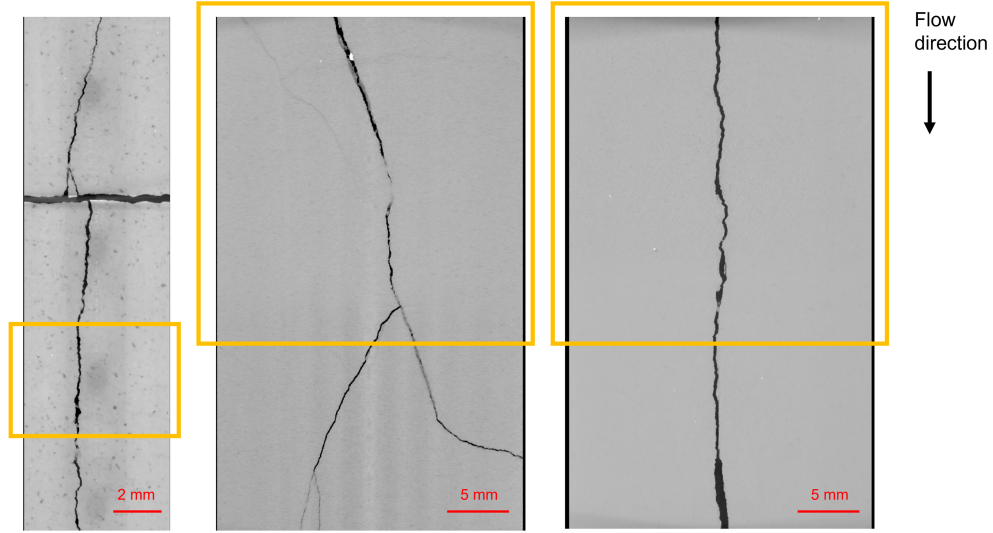
(a)
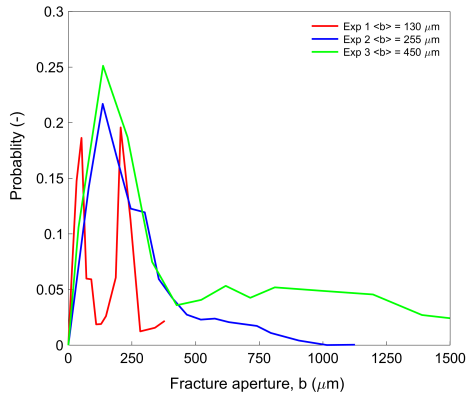
(b)
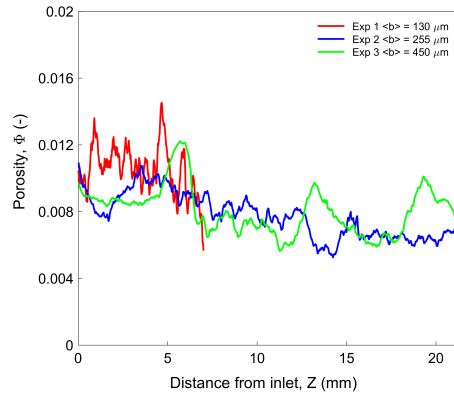
(c)

Figure 2: (a) Dry images of rock samples used in this study. (left) Exp 1: D = 6 mm, $< b > = 130$ µm (middle) Exp 2 : D = 25 mm, $< b > = 255$ µm (right) Exp 3 : D = 25 mm, $< b > = 450$ µm. The yellow box shows the region that is scanned during flow experiments. (b) Fracture aperture distribution for the rock cores in this study. (c) 1-D slice-averaged porosity of rock samples along the length of rock cores in this study.

The absolute permeability is significantly influenced by both fracture aperture and the connectivity of the fracture network. We measure the

14

absolute permeability to water at various flow rates defined by the cubic law described by equation 1. Table 1 summarizes the average porosity and intrinsic fracture permeability of the rock cores. Our findings suggest that porosity does not exhibit a direct proportional relationship with permeability. Instead, it is the fracture network and aperture distribution that predominantly govern fluid flow.

3. Results and discussions

In this section, we first present the in-situ wettability characteristics of different gases derived from X-ray CT images, confirming a water-wet system for all tested cases. Subsequent subsections examine displacement patterns and average saturation profiles, comparing hydrogen and methane. Additionally, we assess the influence of aperture size and roughness on final saturation obtained during drainage, as well as their impact on gas recovery during imbibition. The effects of gas type, aperture variability, and roughness are evaluated in detail to understand their role in fluid displacement dynamics

3.1. Contact angle

The contact angle distribution for drainage from Exp 1 for H_2, CH_4, and the H_2 - CH_4 mixture is shown in Figure 3a. The results indicate a water-wet condition for all gases, with mean contact angles of 57° for hydrogen, 50° for methane, and 49° for the 50 : 50 hydrogen-methane mixture. The contact angle remains fairly consistent across all gases, with a slightly higher value observed for hydrogen. These values align with in situ 3D measurements reported for Bentherimer sandstone [12, 22], where contact angles range from

15

30° to 54°. Other studies employing captive bubble and pendant drop methods have also reported strongly water-wet systems, with contact angles ranging from 27° to 39° on quartz [20]. While X-ray micro-CT measurements are known to overestimate contact angles due to resolution limitations, the relative differences between gases still provide valuable insights [45]. For methane, the contact angles for drainage and imbibition are comparable and within experimental error [12], with values of 50° and 47°, respectively, as shown in Figure 3b.
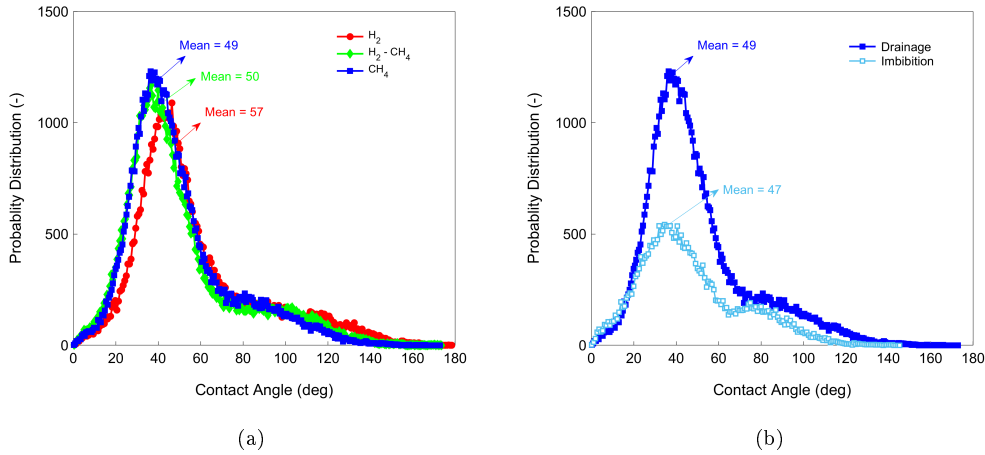
Figure 3: (a) Contact angle distribution after drainage for different gases with brine. Red circles denote H_2, green diamond denote H_2 - CH_4 (50 : 50) mixture and blue squares denote CH_4 (b) Contact angle distribution for CH_4-brine after drainage vs imbibition. Filled squares denote drainage and empty squares denote imbibition

3.2. Drainage displacement dynamics

3.2.1. Effect of gas type : hydrogen versus methane

Figure 4 shows the 3D gas-brine distribution after primary drainage in Exp 1. The flow rate was kept constant for different gases, rather than the capillary number, as the reservoir properties are fixed. However, capil-

lary number is of same order of magnitude for these gases. The observed distribution patterns are consistent across the two pure gases and the gas mixture, which can be attributed to their similar viscosity and interfacial tension values governing flow dynamics. As a result, similar fracture regions are occupied by gas and brine. This observation is further supported by the phase occupancy versus distance data presented in Figure 5. Here, the distance is defined as twice the maximum distance from the center of the aperture to the nearest fracture wall. The data confirm the comparable gas-brine distributions among the tested gases

As gas displaces brine during drainage, it preferentially invades the central regions of the larger apertures, while the brine remains in the narrower apertures and along the fracture walls, as seen in Figure 5 for Exp 1. Notably, regions of gas-brine coexistence within fracture spaces of similar aperture indicate that gas flow is not solely controlled by aperture size but also by the connectivity of larger aperture networks, which facilitate gas propagation. This behavior is consistent with the invasion percolation patterns in water-wet system as reported in fractured media studies [28, 26, 24], where gas flow is dominated by larger, connected pathways with lower capillary entry pressure. Similar trends were observed in Exp 2 and 3, as described in Supplementary Information S4.
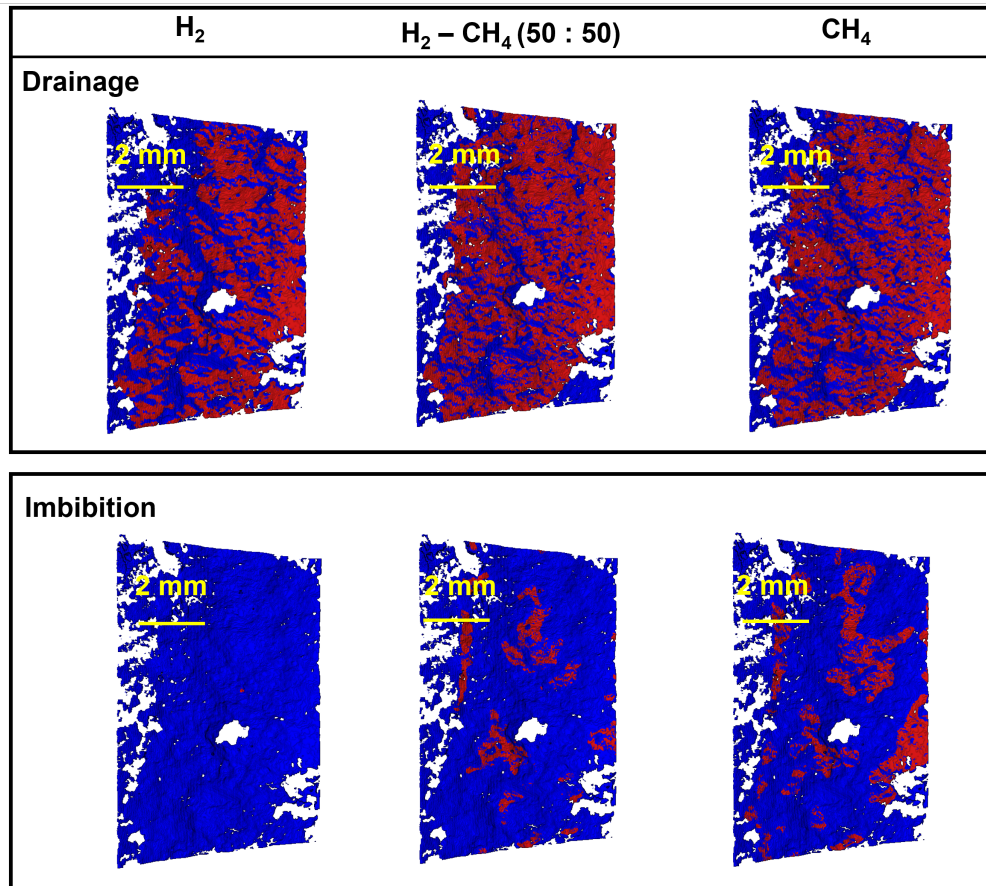
Figure 4: 3-D map of fluid distribution in for different gases after drainage and imbibition for Exp 1 at Ca = 10^{-7}. The red color represent specific gas and blue color represents brine.
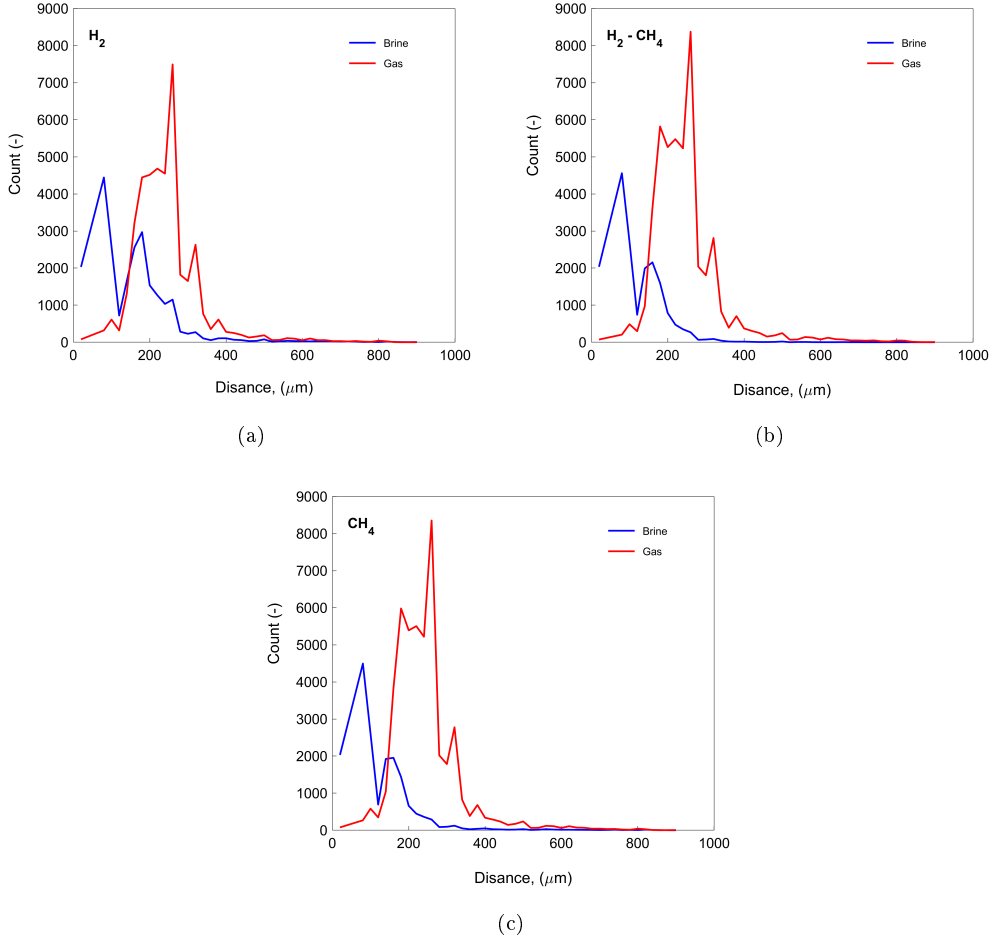
Figure 5: Fluid phase occupancy in Exp 1, D = 6 mm , $< b > = 130$ μm (a) H_2 (b) H_2 - CH_4 (50:50) (c) CH_4. The distance is calculated as twice the maximum distance from the center of the aperture to the nearest wall of the fracture.

The similar behavior observed for all gases is also reflected in the 1-D slice-averaged saturation profiles across all three samples, as shown in Figure 6. The saturation profiles across the fracture for the different gases (H_2, CH_4, and the H_2-CH_4 mixture) demonstrate that, regardless of fracture geometry, the behavior of these gases remains relatively consistent within a given frac-

19

ture, reflected by very similar saturation levels for all gases. It should be noted that these experiments were conducted at similar orders of magnitude for Ca. Methane exhibits slightly higher saturation in Exp 1 and Exp 2 (bottom injection), likely due to its marginally higher viscosity compared to hydrogen, resulting in a higher capillary number (Ca). However, this trend is not observed in Exp 3, where gas is injected from the top, and images are taken near the inlet for both experiments. For wider fracture, gravity effects become more pronounced, which works in the opposite direction as the viscosity-driven trend, leading to higher gas saturation of the lighter gas (H_2 in this case) near the inlet region. The presence of the gravity effect in Exp 3 is further supported by a higher Bond number for Exp 3 compared to Exp 2 (0.06 vs 0.018).
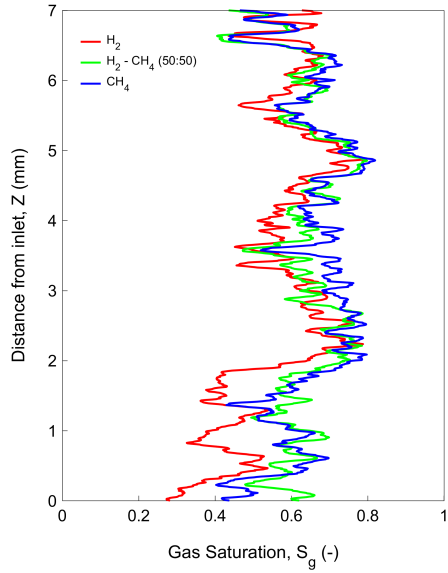
(a)
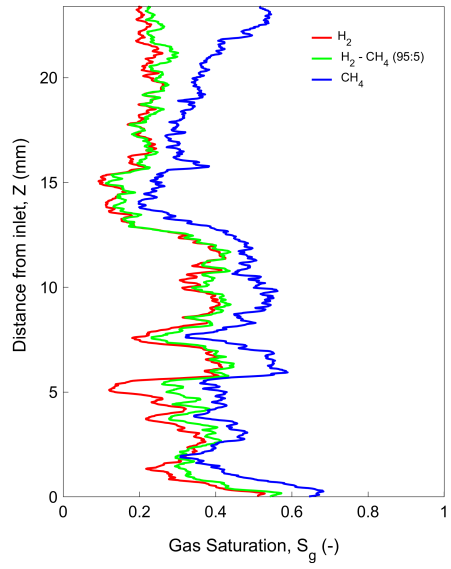
(b)
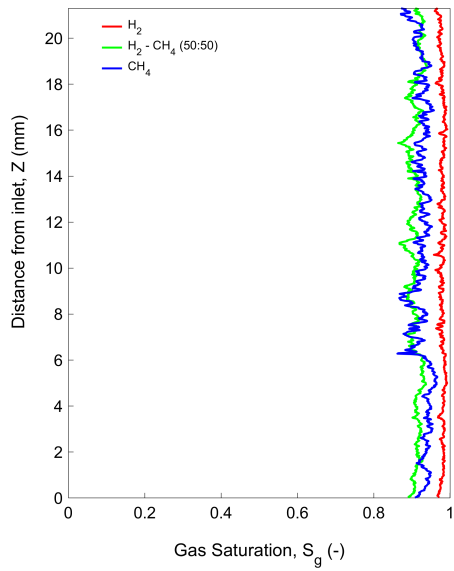
(c)

Figure 6: 1-D slice-average gas saturation after drainage along the length of rock core for different gases. (a) Exp 1, D = 6 mm , $<b> = 130\,\mu$m (b) Exp 2, D = 25 mm , $<b> =$ 255 μm (c) Exp 3, D = 25 mm , $<b> = 450\,\mu$m.

21

Although the average behavior of hydrogen and methane during drainage is similar, there are some pore-scale differences in the mechanisms. Figure 7 (drainage) illustrates the invasion patterns of H_2 and CH_4 at the same capillary number for Exp 2. A key observation is the significantly smaller number of disconnected gas ganglia in the CH_4 invasion compared to H_2. This behavior is attributed to the higher viscosity of methane, which helps stabilize the gas front and reduces break-up events that would otherwise form disconnected ganglia. These break-up events occur when thin brine films drain along the pore walls, but the higher viscosity of gas impedes complete film drainage, stabilizing the gas-brine interface and preventing the wetting phase from breaking the non-wetting phase's continuity [49]. Dynamic phenomena such as roof snap-off events and Haines jumps, which drive these disconnections during capillary-dominated flow, were not directly captured in this study due to the temporal resolution limits of the X-ray scanners. These rapid events have been observed in other studies using synchrotron imaging, where higher temporal resolution can capture the real-time evolution of fluid interfaces during drainage in both porous media [50] and fractured systems [28]
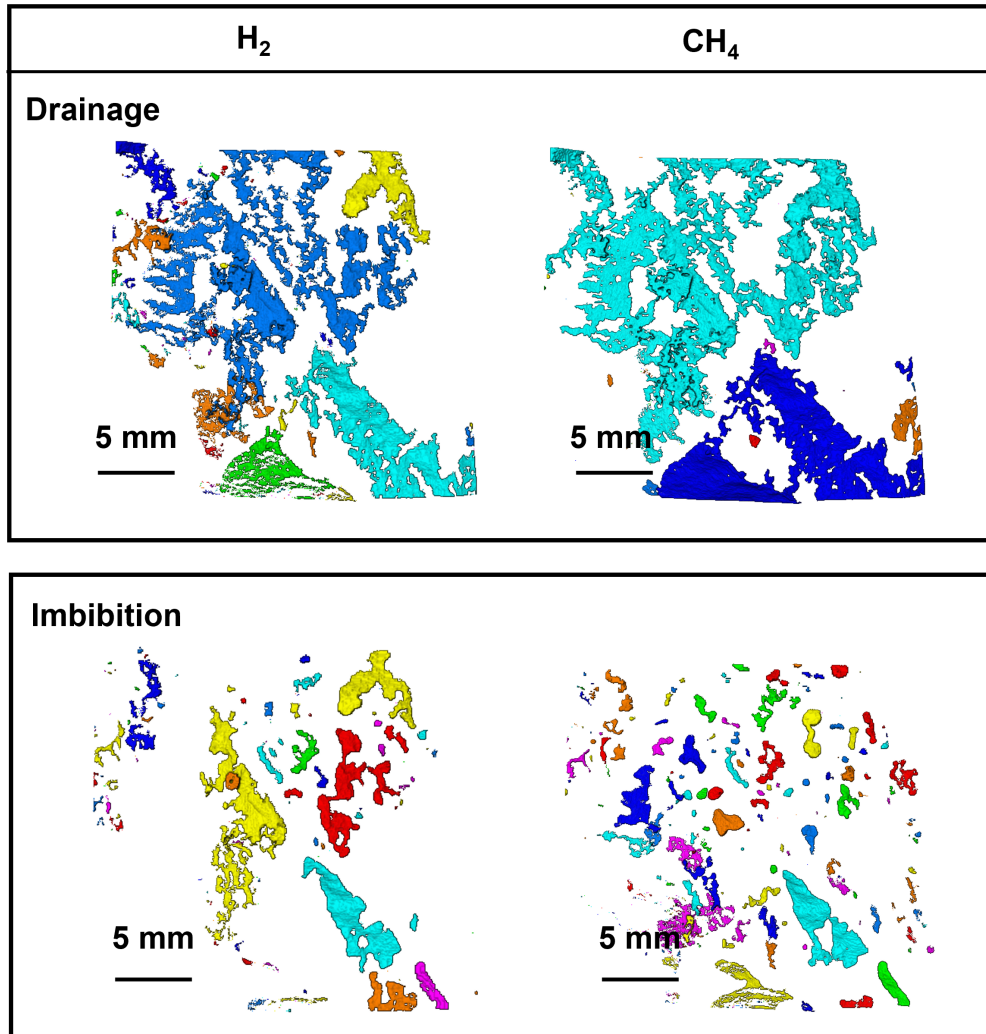
Figure 7: Trapped gas phase for H_2 and CH_4 Exp 2; $< b > = 255$ µm. Each color represents a connected gas ganglia of different size. (Top) after drainage (Bottom) after imbibition

3.2.2. Effect of aperture

Hydrogen and methane exhibit similar behavior within the examined fractured rock samples. It is significantly influenced by the fracture geometry for each gas. Figure 8 (drainage) shows the distribution of H_2 and brine within

23

the fracture after drainage, under similar capillary number conditions for Exp 2 and 3. The gas saturation is significantly higher in the fracture with the larger mean aperture, where $< b > = 450$ µm. In the wider apertures, where the flow resembles stable flow between two parallel plates, nearly all the brine is displaced by the invading gas, resulting in gas saturation exceeding 0.98 (H_2 in this case), with only a thin wetting layer of brine remaining on the fracture surfaces. Figure 9a presents the 1-D saturation profile along the core length for H_2 in both the smaller and larger aperture fractures. In narrower fracture of Exp 2 with a mean aperture of $< b > = 255$ µm, the average gas saturation is approximately 0.27%. A wider aperture corresponds to a lower capillary entry pressure, enabling the gas to displace more brine from the pore space. As a result, the gas saturation is markedly higher in wider fractures, where gas can more easily invade and occupy the fracture volume. Similar trends are observed for methane as shown in Supplementary Information S5.
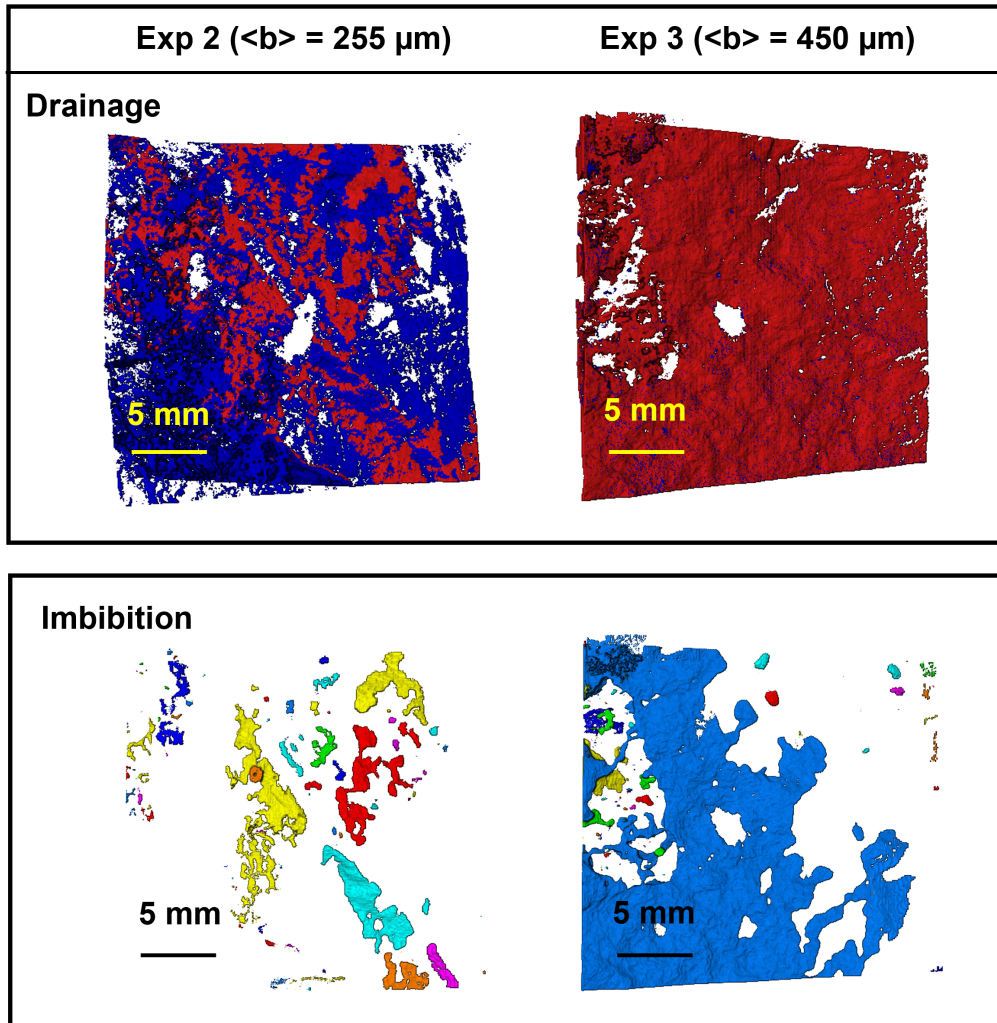
Figure 8: (Top) 3-D map of H_2 - brine distribution after drainage for Exp 2 and 3. The red color represent specific gas and blue color represents brine. (Bottom) 3-D volume rendering of discrete ganglia trapped in the fracture after imbibition for Exp 2 and 3. Each color represents a connected gas ganglia of different size.
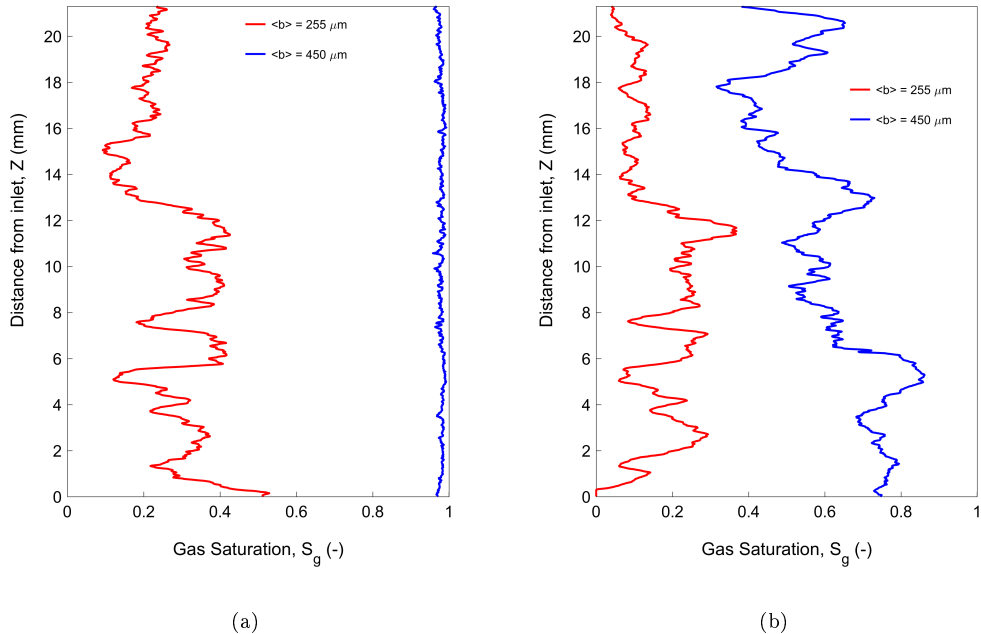
Figure 9: 1-D slice-average gas saturation H_2 for cores with different fracture aperture size. The red line denotes saturation for Exp 2 : D = 25 mm, $< b > = 255$ µm. The blue line denotes the saturation for Exp 3: D = 25 mm, $< b > = 450$ µm. (a) after drainage (b) after imbibition.

3.2.3. Effect of roughness

We define roughness as the irregularity in aperture and branching from the primary fracture. Although the capillary numbers and viscosity ratios are similar across all experiments, the results from Exp 2 differ due to the complexity of the fracture geometry. In Exp 2, gas saturation is significantly lower ($S_g = 0.27$) compared to Exp 1 and Exp 3, where higher gas saturations are observed ($S_g = 0.57$ for Sample 1 and $S_g = 0.98$ for Sample 3) after drainage. The reduced gas saturation in Exp 2 arises from more disconnected gas ganglia, likely caused by snap-off events due to the higher roughness of the rock sample. In contrast, Samples 1 and 3, with smoother surfaces, exhibit

26

more connected invasion patterns, as shown in Figure 10 (top). As discussed in Section 3.2.2, the lower gas saturation in Sample 2 compared to Sample 3 is partly attributed to its narrower aperture size. However, Sample 1, despite having a narrower mean aperture ($\langle b \rangle = 130$ µm), achieved notably higher gas saturation. This highlights the significant influence of roughness on gas displacement. Similar disconnected complex invasion patterns are observed for decane-brine fluids through rough fractures [28]. While decoupling the effects of aperture size and roughness remains challenging due to the inherent variability in the studied samples, the observed trends provide valuable qualitative insights.
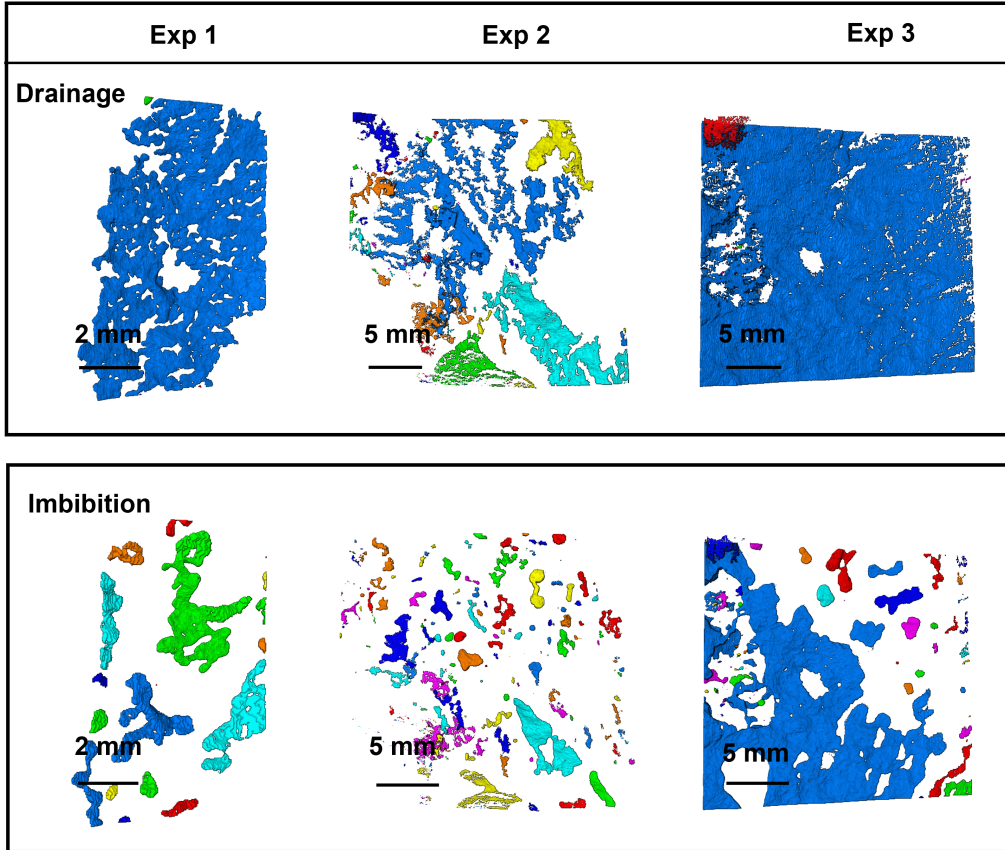
Figure 10: (Top) 3-D volume rendering of H_2 discrete ganglia after drainage for Exp 1, 2 and 3. (Bottom) 3-D volume rendering of CH_4 discrete ganglia trapped in the fracture after imbibition for Exp 1, 2 and 3. Each color represents a connected gas ganglia of different size.

3.3. Imbibition and trapping

When brine re-enters the fracture during the imbibition process, it displaces the gas, typically resulting in gas being trapped in the form of discrete ganglia. These ganglia impede the efficient recovery of stored energy in underground storage operations, making the study of imbibition mechanisms crucial. During imbibition, the capillary number and viscosity ratio are significantly higher than during drainage due to brine's greater viscosity, as

shown in the phase diagram Figure S1. The flow rate, constrained by experimental limitations, prevented achieving the lower capillary numbers observed in drainage.

3.3.1. Effect of gas type : hydrogen versus methane

Figure 4 (bottom) illustrates the 3-D gas-brine distribution for Exp 1; rock core with a mean aperture $< b > = 130$ µm, where imbibition is conducted at a capillary number of $Ca = 10^{-5}$ for the different gases. For H_2, gas is fully displaced from the fracture, resulting in a 100% recovery of the stored gas. In contrast, substantial gas remains trapped in the fracture when methane and the 50 : 50 H_2-CH_4 mixture are used. The 1-D gas saturation profile in Figure 11a shows a higher recovery of 75% for the 50 : 50 H_2 - CH_4 mixture, compared to 58% for pure CH_4. The 100% recovery of hydrogen is notable as there is typically some residual trapped gas in the fracture or porous media [51, 52]. This is unexpected and might be a dissolution effect as it is observed in previous studies [18, 53]. This indicates that the types of gas has greater impact on imbibition compared to drainage, especially at slightly higher capillary number of $Ca = 10^{-5}$.
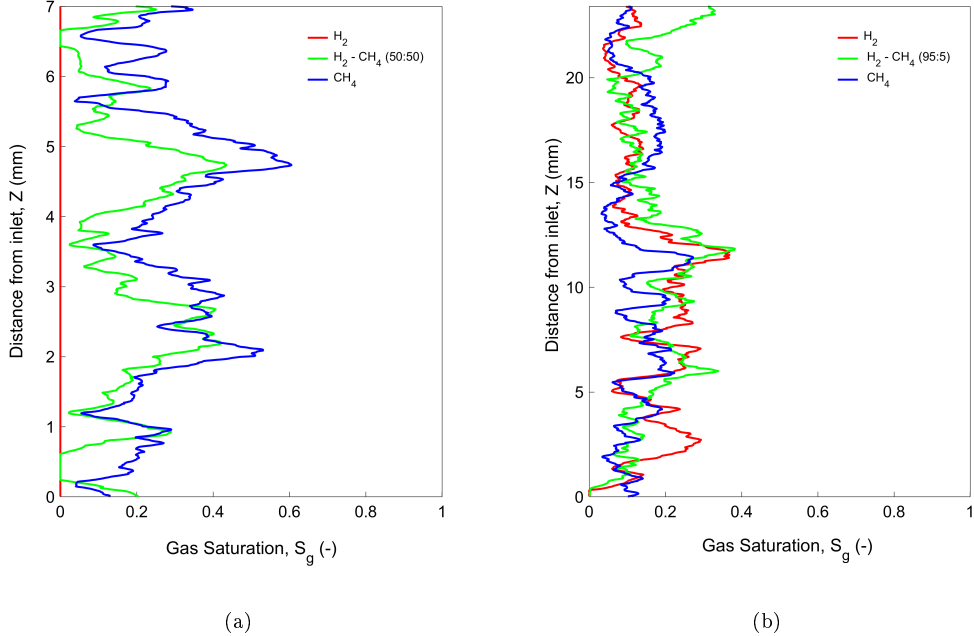
Figure 11: 1-D slice-average gas saturation after imbibition. (a) Exp 1 : $<b> = 130$ µm (b) Exp 2 : $<b> = 255$ µm.

However, at lower capillary numbers, as observed in Exp 2 with $Ca = 10^{-6}$, where capillary forces dominate, the influence of gas type on imbibition becomes less pronounced. Additionally, it is important to note that the sample size differs, with Exp 2 using a 25 mm sample compared to the 6 mm sample in Exp 1, along with a slightly different setup, which could also influence the results. As shown in Figure 11b, the gas saturation after imbibition remains comparable across gases, with slight variation; 0.15 for H_2, 0.17 for 95% H_2 and 5% CH_4 mixture and 0.13 for CH_4. Similar trends are observed for Sample 3, as discussed in Supplementary Information S6. These minor differences fall within experimental uncertainty, indicating that the gas type has limited influence under capillary-dominated conditions. This finding is

significant for underground gas storage, as residual gas can influence relative permeability, which in turn affects pressure cycling during storage and retrieval operations.

To explore the detailed mechanisms underlying the differences in imbibition of H_2 and CH_4, the trapped gas phase was analyzed, as shown in Figure 7 (bottom) for Exp 2. The results reveal a larger number of small-sized ganglia for methane compared to hydrogen. This could be attributed to dissolution and Ostwald ripening, where smaller gas ganglia disappear while medium-sized ganglia grow. This process occurs more rapidly for hydrogen compared to methane, likely due to hydrogen's lower viscosity and smaller molecular size. Further investigation is needed to explore this phenomenon in more detail. A similar pattern is observed for the wider fracture sample in Exp 3 ($< b > = 450$ µm), as detailed in Supplementary Information S7.

3.3.2. Effect of aperture size and roughness

The impact of fracture aperture on imbibition was evaluated similarly to drainage. The results show that the gas phase remains better connected and harder to displace in Exp 3 with wider fractures, $< b > = 450$ µm, as shown in Figure 8 (bottom). This suggests that gas recovery is more difficult in wider aperture fractures. In these fractures, brine tends to flow along the fracture walls as a thin film, while larger gas bubbles remain trapped in the center of the fracture, making it harder to displace the gas. After drainage in Exp 3, sample with a wider fracture, achieves a significantly higher gas saturation of $S_g = 0.98$ for hydrogen compared to Exp 2, $S_g = 0.27$ (Figure 9a). However, following imbibition, Sample 2 exhibits better gas recovery of 44% compared to 37% Sample i3 as shown in Figure 9b. Consequently,

31

the residual gas saturation remains significantly higher in the larger aperture fracture, at $S_g = 0.6$. compared to just $S_g = 0.15$ in the narrower fracture. This disparity may also be influenced by fracture roughness.

Figure 10 (bottom) illustrates the trapped methane ganglia after imbibition for the three samples. Sample 2, with the highest roughness, has the most and smallest methane ganglia. Sample 1 shows fewer, less connected ganglia, while sample C has the least fragmented clusters. The aperture size also influences gas trapping, with larger apertures leading to higher residual gas saturation. However, the fewer connected ganglia in sample 1, despite its narrower aperture, indicate that fracture roughness plays a significant role in disconnection during imbibition. It could also be possible that Ostwald ripening plays a bigger role in this smaller sample, because length scale is smaller and maybe also because there's less brine so the dissolved concentration is influenced more easily. This effect is reflected in gas recovery efficiencies: sample 3 achieves 38%, sample 1 50%, and sample 2 the highest at 70%. Notably, imbibition for sample 1 was performed at an order of magnitude higher capillary number, resulting in 100% recovery for hydrogen. Direct comparison and decoupling of roughness effects are therefore challenging. However, the lower recovery for sample 1, even at higher Ca (where higher Ca typically improves recovery), underscores the critical influence of fracture roughness on gas trapping and disconnection.

4. Conclusions and implications

This study provides fundamental insights into the pore-scale two-phase flow dynamics of hydrogen (H_2), methane (CH_4), and their mixtures dur-

ing drainage (injection) and imbibition (withdrawal) in fractured rocks, with particular relevance to converting the existing natural gas facility at Loenhout to hydrogen storage. We conducted controlled drainage and imbibition core-flood experiments for these gases at reservoir pressure (10 MPa) and temperature (65°C) on three fractured rocks with varying aperture and roughness.

Overall, our paper establishes the following key conclusions:

1. H_2 and the H_2 - CH_4 mixture, as well as CH_4, exhibit fairly similar fluid distribution and saturation profiles after drainage in the capillary-dominated flow regime. Methane achieves slightly higher gas saturation during drainage compared to hydrogen, likely due to its higher viscosity. The displacement mechanism reveals that gas invades in disconnected clusters due to snap-off events, which are more pronounced for hydrogen compared to methane, likely due to methane's higher viscosity as reported by previous studies [50, 28].

2. For imbibition, at a higher capillary number (Ca = 10^{-5}) in smaller sample 6 mm hydrogen shows 100% gas recovery, in contrast to significant residual gas trapping observed in the 50:50 H_2 and CH_4 mixture (S_g = 0.16) and CH_4 (S_g = 0.27). 100% recovery in case of hydrogen could be dissolution effect as observed in previous studies [18, 53]. Whereas in larger diameter samples 25 mm where experiments are performed at slightly lower capillary number (Ca = 10^{-6}), hydrogen and methane exhibit similar fracture-specific behavior. However, methane forms more fragmented and smaller size ganglia than hydrogen.

3. Fracture aperture influences both gas saturation after drainage and imbibition. Wider fractures exhibit higher gas saturations during drainage but lower recovery efficiencies during imbibition, as gas remains connected and brine flows along the fracture wall surrounding the large gas clusters.

4. Fractures with higher roughness show more disconnected gas clusters during both drainage and imbibition, which affects the final gas saturation profiles.

These findings provide important insights into gas flow mechanisms in fractured reservoirs, underscoring the importance of considering gas type, fracture geometry, capillary number, and snap-off dynamics when designing efficient underground hydrogen storage systems. The observed similarities between hydrogen and methane indicate that converting existing natural gas storage facilities to hydrogen storage would require minimal adjustments for flow properties. However, further research is needed to address upscaling in larger fracture networks. A key consideration is the impact of fracture aperture and roughness. Wider fractures with less variability in aperture distribution achieve higher gas saturation during drainage, potentially indicating greater storage capacity. However, this can be misleading, as these fractures exhibit significantly lower recovery efficiency. Consequently, both fracture aperture and roughness must be carefully incorporated into field-scale models to optimize storage capacity and recovery processes

In the recovery cycle, our experiments show that at higher capillary numbers and a smaller sample size of 6 mm, which are associated with increased

recovery rates, hydrogen achieves nearly 100% recovery. This could be attributed to the smaller scale of the samples, suggesting potential experimental effects influencing the results.

In conclusion, our findings emphasize the importance of studying hydrogen-brine flow through rough fractures, as the flow dynamics are critically influenced by both fracture geometry and fluid properties. The time scales associated with dissolution and Ostwald ripening need further exploration to better understand the pore-scale dynamics of disconnected ganglia. These insights are crucial for improving upscaled models of permeability and trapping, which are essential for optimizing underground hydrogen storage (UHS).

Acknowledgments

References

[1] Davood Zivar, Sunil Kumar, and Jalal Foroozesh. Underground hydrogen storage: A comprehensive review. *International Journal of Hydro-*

gen Energy, 46(45):23436–23462, 2021. doi: https://doi.org/10.1016/j. ijhydene.2020.08.138.

[2] Humza Bin Navaid, Hossein Emadi, and Marshall Watson. A comprehensive literature review on the challenges associated with underground hydrogen storage. *International Journal of Hydrogen Energy*, 48(28): 10603–10635, 2023. ISSN 03603199. doi: 10.1016/j.ijhydene.2022.11. 225. URL https://doi.org/10.1016/j.ijhydene.2022.11.225.

[3] R. Tarkowski and B. Uliasz-Misiak. Towards underground hydrogen storage: A review of barriers. *Renewable and Sustainable Energy Reviews*, 162:112451, 2022. doi: https://doi.org/10.1016/j.rser.2022. 112451.

[4] Leila Hashemi, Martin Blunt, and Hadi Hajibeygi. Pore-scale modelling and sensitivity analyses of hydrogen-brine multiphase flow in geological porous media. *Scientific Reports*, 11(1):1–13, 2021. doi: https://doi. org/10.1038/s41598-021-87490-7.

[5] Arshad Raza, Muhammad Arif, Guenther Glatz, Mohamed Mahmoud, Mohammed Al Kobaisi, Saad Alafnan, and Stefan Iglauer. A holistic overview of underground hydrogen storage: Influencing factors, current understanding, and outlook. *Fuel*, 330:125636, 2022. doi: https://doi. org/10.1016/j.fuel.2022.125636.

[6] Nasiru Salahu Muhammed, Bashirul Haq, Dhafer Al Shehri, Amir Al-Ahmed, Mohammed Mizanur Rahman, and Ehsan Zaman. A review on underground hydrogen storage: Insight into geological sites, influencing

factors and future outlook. *Energy Reports*, 8:461–499, 2022. doi: https://doi.org/10.1016/j.egyr.2021.12.002.

[7] M W Melaina, O. Antonia, and M. Penev. Blending Hydrogen into Natural Gas Pipeline Networks: A Review of Key Issues. Technical Report NREL/TP-5600-51995, National Renewabler Energy Laboratory. *Contract*, 303(March):275–3000, 2013. doi: http://www.osti.gov/servlets/purl/1068610/.

[8] Andrew Cavanagh, Hamid Yousefi, Mark Wilkinson, and Remco Groenenberg. Hydrogen storage potential of existing european gas storage sites in depleted gas fields and aquifers. Technical report, June 2022.

[9] Adnan Aftab, Aliakbar Hassanpouryouzband, Quan Xie, Laura L. Machuca, and Mohammad Sarmadivaleh. Toward a Fundamental Understanding of Geological Hydrogen Storage. *Industrial and Engineering Chemistry Research*, 61(9):3233–3253, 2022. doi: https://doi.org/10.1021/acs.iecr.1c04380.

[10] Masoud Aslannezhad, Muhammad Ali, Azim Kalantariasl, Mohammad Sayyafzadeh, Zhenjiang You, Stefan Iglauer, and Alireza Keshavarz. A review of hydrogen/rock/brine interaction: Implications for Hydrogen Geo-storage. *Progress in Energy and Combustion Science*, 95:101066, 2023. doi: https://doi.org/10.1016/j.pecs.2022.101066.

[11] Sojwal Manoorkar, Gülce Kalyoncu Pakkaner, Hamdi Omar, Soetkin Barbaix, Dominique Ceursters, Maxime Latinis, Stefanie Van Offenwert, and Tom Bultreys. From underground natural gas to hydrogen storage in

fractured reservoir rock: comparing relative permeabilities for hydrogen versus methane and nitrogen. *arXiv preprint arXiv:2411.14122*, 2024.

[12] Zaid Jangda, Hannah Menke, Andreas Busch, Sebastian Geiger, Tom Bultreys, Helen Lewis, and Kamaljit Singh. Pore-scale visualization of hydrogen storage in a sandstone at subsurface pressure and temperature conditions: Trapping, dissolution and wettability. *Journal of Colloid and Interface Science*, 629(Part B):316–325, 2023. doi: https://doi.org/10.1016/j.jcis.2022.09.082.

[13] Sepideh Goodarzi, Yihuai Zhang, Sajjad Foroughi, Branko Bijeljic, and Martin J. Blunt. Trapping, hysteresis and Ostwald ripening in hydrogen storage: A pore-scale imaging study. *International Journal of Hydrogen Energy*, 56(December 2023):1139–1151, 2024. ISSN 03603199. doi: 10.1016/j.ijhydene.2023.12.029.

[14] Eike M. Thaysen, Ian B. Butler, Aliakbar Hassanpouryouzband, Damien Freitas, Fernando Alvarez-Borges, Samuel Krevor, Niklas Heinemann, Robert Atwood, and Katriona Edlmann. Pore-scale imaging of hydrogen displacement and trapping in porous media. *International Journal of Hydrogen Energy*, 48(8):3091–3106, 2023. doi: https://doi.org/10.1016/j.ijhydene.2022.10.153.

[15] Robert J. Glass, Harihar Rajaram, and Russell L. Detwiler. Immiscible displacements in rough-walled fractures: Competition between roughening by random aperture variations and smoothing by in-plane curvature. *Physical Review E - Statistical Physics, Plasmas, Fluids, and*

Related Interdisciplinary Topics, 68(6):1–6, 2003. ISSN 1063651X. doi: 10.1103/PhysRevE.68.061110.

[16] Russell L. Detwiler, Harihar Rajaram, and Robert J. Glass. Satiated relative permeability of variable-aperture fractures. *Physical Review E*, 71(3):031114, mar 2005. ISSN 1539-3755. doi: 10.1103/PhysRevE.71. 031114.

[17] Zhibing Yang, Insa Neuweiler, Yves Méheust, Fritjof Fagerlund, and Auli Niemi. Fluid trapping during capillary displacement in fractures. *Advances in Water Resources*, 95:264–275, 2016. doi: http://dx.doi.org/ 10.1016/j.advwatres.2015.07.015.

[18] Maartje Boon and Hadi Hajibeygi. Experimental characterization of H 2 /water multiphase flow in heterogeneous sandstone rock at the core scale relevant for underground hydrogen storage (UHS). *Scientific Reports*, 12(1):1–12, 2022. doi: https://doi.org/10.1038/s41598-022-18759-8.

[19] Zhenkai Bo, Maartje Boon, Hadi Hajibeygi, and Suzanne Hurter. Impact of experimentally measured relative permeability hysteresis on reservoir-scale performance of underground hydrogen storage (UHS). *International Journal of Hydrogen Energy*, 48(36):13527–13542, 2023. doi: https://doi.org/10.1016/j.ijhydene.2022.12.270.

[20] Scott Higgs, Ying Da Wang, Chenhao Sun, Jonathan Ennis-King, Samuel J. Jackson, Ryan T. Armstrong, and Peyman Mostaghimi. In-situ hydrogen wettability characterisation for underground hydrogen

storage. *International Journal of Hydrogen Energy*, 47(26):13062–13075, 2022. doi: https://doi.org/10.1016/j.ijhydene.2022.02.022.

[21] Yihuai Zhang, Branko Bijeljic, Ying Gao, Sepideh Goodarzi, Sajjad Foroughi, and Martin J. Blunt. Pore-Scale Observations of Hydrogen Trapping and Migration in Porous Rock: Demonstrating the Effect of Ostwald Ripening. *Geophysical Research Letters*, 50(7):1–8, 2023. ISSN 19448007. doi: 10.1029/2022GL102383.

[22] Scott Higgs, Ying Da Wang, Chenhao Sun, Jonathan Ennis-King, Samuel J. Jackson, Ryan T. Armstrong, and Peyman Mostaghimi. Comparative analysis of hydrogen, methane and nitrogen relative permeability: Implications for Underground Hydrogen Storage. *Journal of Energy Storage*, 73(Part C):108827, 2023. doi: https://doi.org/10.1016/j.est.2023.108827.

[23] P. Persoff and K. Pruess. Two-Phase Flow Visualization and Relative Permeability Measurement in Natural Rough-Walled Rock Fractures. *Water Resources Research*, 31(5):1175–1186, 1995. doi: https://doi.org/10.1029/95WR00171.

[24] Z. T. Karpyn, A. S. Grader, and P. M. Halleck. Visualization of fluid occupancy in a rough fracture using micro-tomography. *Journal of Colloid and Interface Science*, 307(1):181–187, 2007. doi: https://doi.org/10.1016/j.jcis.2006.10.082.

[25] Ran Hu, Chen Xing Zhou, Dong Sheng Wu, Zhibing Yang, and Yi Feng Chen. Roughness Control on Multiphase Flow in Rock Fractures. *Geo-*

physical Research Letters, 46(21):12002–12011, 2019. ISSN 19448007. doi: 10.1029/2019GL084762.

[26] Yi Feng Chen, Shu Fang, Dong Sheng Wu, and Ran Hu. Visualizing and quantifying the crossover from capillary fingering to viscous fingering in a rough fracture. *Water Resources Research*, 53(9):7756–7772, 2017. doi: https://doi.org/10.1002/2017WR021051.

[27] Tomos Phillips, Tom Bultreys, Kevin Bisdom, Niko Kampman, Stefanie Van Offenwert, Arjen Mascini, Veerle Cnudde, and Andreas Busch. A Systematic Investigation Into the Control of Roughness on the Flow Properties of 3D-Printed Fractures. *Water Resources Research*, 57(4): 1–23, 2021. ISSN 19447973. doi: 10.1029/2020WR028671.

[28] Tomos Phillips, Tom Bultreys, Jeroen van Stappen, Kamaljit Singh, Erik Clemens Boersheim, Sahyuo Achuo Dze, Stefanie von Offenwert, Ben Callow, Mostafa Borji, Vladimir Novak, Christian M. Schlepütz, Veerle Cnudde, Florian Doster, and Andreas Busch. Influence of Local Aperture Heterogeneity on Invading Fluid Connectivity During Rough Fracture Drainage. *SSRN Electronic Journal*, 151:2387–2403, 2023. doi: https://doi.org/10.1007/s11242-024-02117-5.

[29] M. Fourar, S. Bories, R. Lenormand, and P. Persoff. Two-phase flow in smooth and rough fractures: Measurement and correlation by porous-medium and pipe flow models. *Water Resources Research*, 29(11):3699–3708, 1993. ISSN 19447973. doi: 10.1029/93WR01529.

[30] M Fourar. Experimental study of air-water two-phase flow through a

fracture (narrow channel). *International Journal of Multiphase Flow*, 22 (4):122, 1996. ISSN 03019322. doi: 10.1016/s0301-9322(97)88370-x.

[31] Zhibing Yang, Auli Niemi, Fritjof Fagerlund, and Tissa Illangasekare. Two-phase flow in rough-walled fractures: Comparison of continuum and invasion-percolation models. *Water Resources Research*, 49(2):993–1002, 2013. doi: https://doi.org/10.1002/wrcr.20111.

[32] R. G. Hughes and M. J. Blunt. Network modeling of multiphase flow in fracture. *Advances in Water Resources*, 24(3-4):409–421, 2001. ISSN 03091708. doi: 10.1016/S0309-1708(00)00064-6.

[33] Zhi Dou, Zhifang Zhou, and B.E. Sleep. Influence of wettability on interfacial area during immiscible liquid invasion into a 3D self-affine rough fracture: Lattice Boltzmann simulations. *Advances in Water Resources*, 61:1–11, nov 2013. doi: https://doi.org/10.1016/j.advwatres.2013.08.007.

[34] Mohammad Piri and Zuleima T. Karpyn. Prediction of fluid occupancy in fractures using network modeling and x-ray microtomography. II: Results. *Physical Review E - Statistical, Nonlinear, and Soft Matter Physics*, 76(1):016316, 2007. doi: https://doi.org/10.1103/PhysRevE.76.016316.

[35] Chih Ying Chen and Roland N. Horne. Two-phase flow in rough-walled fractures: Experiments and a flow structure model. *Water Resources Research*, 42(3):1–17, 2006. doi: https://doi.org/10.1029/2004WR003837.

[36] Roland Dreesen, Jos Bouckaert, Michiel Dusar, J Soille, and Noël Vandenberghe. Subsurface structural analysis of the late-Dinantian carbonate shelf at the northern flank of the Brabant Massif (Campine Basin, N-Belgium). *Mémoires pour servir à l'Explication des Cartes Géologiques et Minières de la Belgique*, 21:1–37, 1987.

[37] David Lagrou and Ben Laenen. Introduction of new formal lithographic units for the Dinantian in the Campine Basin. In *In Proceedings of the 4th International Geologica Belgica Meeting*, pages 11–14, 2012.

[38] Eva van der Voet, Philippe Muchez, Ben Laenen, Gert Jan Weltje, David Lagrou, and Rudy Swennen. Characterizing carbonate reservoir fracturing from borehole data – A case study of the Viséan in northern Belgium. *Marine and Petroleum Geology*, 111:375–389, 2020. doi: https://doi.org/10.1016/j.marpetgeo.2019.08.040.

[39] Roland Lenormand, Eric Touboul, and Cesar Zarcone. Numerical models and experiments on immiscible displacements in porous media. *Journal of Fluid Mechanics*, 189(November):165–187, 1988. ISSN 14697645. doi: 10.1017/S0022112088000953.

[40] Manuel Dierick, Denis Van Loo, Bert Masschaele, Jan Van Den Bulcke, Joris Van Acker, Veerle Cnudde, and Luc Van Hoorebeke. Recent micro-CT scanner developments at UGCT. *Nuclear Instruments and Methods in Physics Research, Section B: Beam Interactions with Materials and Atoms*, 324:35–40, 2014. doi: http://dx.doi.org/10.1016/j.nimb.2013.10.051.

[41] Bert Masschaele, Manuel Dierick, Denis Van Loo, Matthieu N. Boone, Loes Brabant, Elin Pauwels, Veerle Cnudde, and Luc Van Hoorebeke. HECTOR: A 240kV micro-CT setup optimized for research. *Journal of Physics: Conference Series*, 463:012012, 2013. doi: 10.1088/1742-6596/463/1/012012.

[42] Jeff Gostick, Zohaib Khan, Thomas Tranter, Matthew Kok, Mehrez Agnaou, Mohammadamin Sadeghi, and Rhodri Jervis. PoreSpy: A Python Toolkit for Quantitative Analysis of Porous Media Images. *Journal of Open Source Software*, 4(37):1296, 2019. doi: https://doi.org/10.21105/joss.01296.

[43] Ahmed AlRatrout, Ali Q. Raeini, Branko Bijeljic, and Martin J. Blunt. Automatic measurement of contact angle in pore-space images. *Advances in Water Resources*, 109:158–169, 2017. ISSN 03091708. doi: 10.1016/j.advwatres.2017.07.018.

[44] Ahmed AlRatrout, Martin J. Blunt, and Branko Bijeljic. Wettability in complex porous materials, the mixed-wet state, and its relationship to surface roughness. *Proceedings of the National Academy of Sciences of the United States of America*, 115(36):8901–8906, 2018. ISSN 10916490. doi: 10.1073/pnas.1803734115.

[45] Ahmed AlRatrout, Martin J. Blunt, and Branko Bijeljic. Spatial Correlation of Contact Angle and Curvature in Pore-Space Images. *Water Resources Research*, 54(9):6133–6152, 2018. doi: 10.1029/2017WR022124.

[46] Nick Barton and Eda F De Quadros. Joint aperture and roughness

in the prediction of flow and groutability of rock masses. *nternational Journal of Rock Mechanics and Mining Sciences*, 3-4(252-e1), 1997. doi: https://doi.org/10.1016/S1365-1609(97)00081-6.

[47] Lichun Wang and M. Bayani Cardenas. Transition from non-Fickian to Fickian longitudinal transport through 3-D rough fractures: Scale-(in)sensitivity and roughness dependence. *Journal of Contaminant Hydrology*, 198:1–10, 2017. doi: http://dx.doi.org/10.1016/j.jconhyd.2017.02.002.

[48] Zuyang Ye, Hui Hai Liu, Qinghui Jiang, and Chuangbing Zhou. Two-phase flow properties of a horizontal fracture: The effect of aperture distribution. *Advances in Water Resources*, 76:43–54, 2015. doi: http://dx.doi.org/10.1016/j.advwatres.2014.12.001.

[49] Martin J. Blunt. *Multiphase flow in permeable media: a pore-scale perspective*. Cambridge university press. doi: https://doi.org/10.1017/9781316145098.

[50] Catherine Spurin, Maja Rücker, Marcel Moura, Tom Bultreys, Gaetano Garfi, Steffen Berg, Martin J. Blunt, and Samuel Krevor. Red Noise in Steady-State Multiphase Flow in Porous Media. *Water Resources Research*, 58(7):1–8, 2022. doi: https://doi.org/10.1029/2022WR031947.

[51] Catriona A Reynolds and Samuel Krevor. Characterizing flow behavior for gas injection: Relative permeability of CO2-brine and N2-water in heterogeneous rocks. *JAWRA Journal of the American Water Resources*

Association, 5(3):2–2, 1969. ISSN 1093-474X. doi: 10.1111/j.1752-1688.
1969.tb04897.x.

[52] Samuel J. Jackson, Simeon Agada, Catriona A. Reynolds, and Samuel
Krevor. Characterizing Drainage Multiphase Flow in Heterogeneous
Sandstones. *Water Resources Research*, 54(4):3139–3161, 2018. ISSN
19447973. doi: 10.1029/2017WR022282.

[53] Maartje Boon, Tim Rademaker, Chandra Widyananda Winardhi, and
Hadi Hajibeygi. Multiscale experimental study of h_2/brine multiphase
flow in porous rock characterizing relative permeability hysteresis, hy-
drogen dissolution, and ostwald ripening. *Scientific Reports*, 14(1):1–15,
2024. doi: https://doi.org/10.1038/s41598-024-81720-4.

Supplementary Information for: "The role of microscopic displacement dynamics for underground hydrogen versus natural gas storage in fractured reservoirs"

Sojwal Manoorkar[a,b,*], Gülce Kalyoncu Pakkaner[a,b], Hamdi Omar[a,b], Soetkin Barbaix[a,b], Dominique Ceursters[c], Maxime Latinis[c], Stefanie Van Offenwert[c], Tom Bultreys[a,b]

[a]*Department of Geology, Ghent University, Ghent, Belgium*
[b]*Centre for X-ray Tomography (UGCT), Ghent University, Ghent, Belgium*
[c]*Fluxys, Belgium*

Contents

- Section S1: Flow parameters

- Section S2: Theory and definitions

- Section S3: Detailed experimental procedure

- Section S4: Fluid occupancy for large samples from Exp 2 and 3

- Section S5: Effect of aperture for CH_4 - brine distribution after drainage

- Section S6: Saturation for Exp 3 after imbibition

---

*I am corresponding author
Email address: sojwal.manoorkar@Ugent.be/sojwal.m@gmail.com (Sojwal Manoorkar)

- Section S7: Disconnected gas ganglia after imbition in Exp 3

1. Section 1: Flow parameters

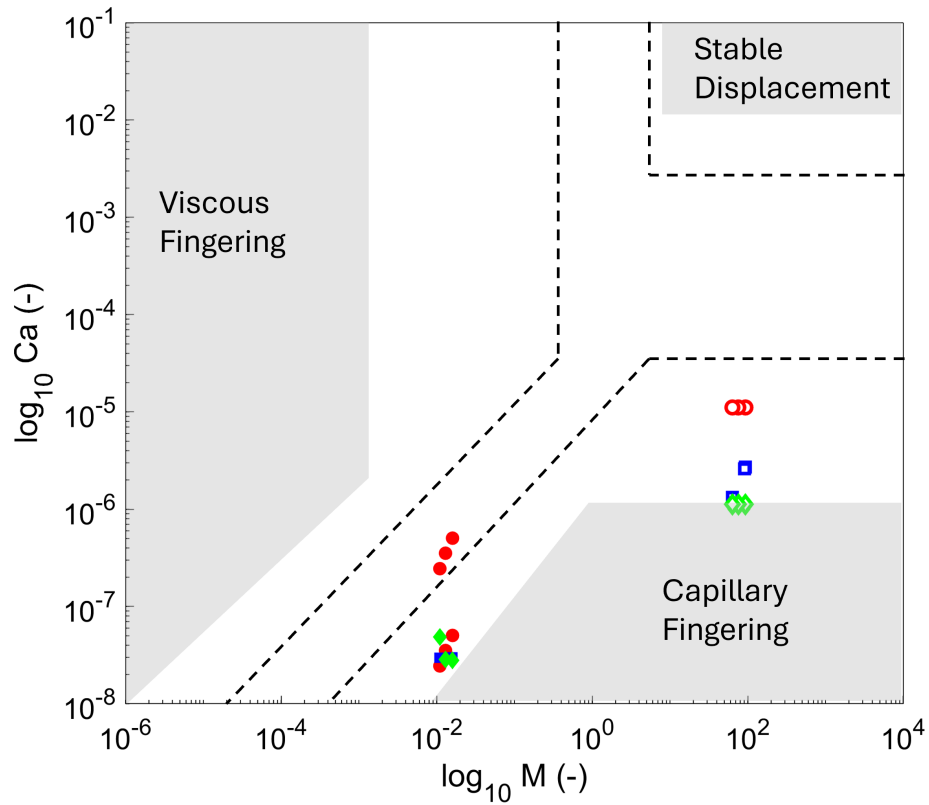The flow parameters Capillary number and viscosity ratio or all the experiments performed in this study.

Figure S1: Capillary number (Ca) and viscosity ratio (M) for drainage studied in this paper overlayed on phase diagram for porous media [1]. The filled markers represent drainage experiments, while the empty markers correspond to imbition experiments. Red circles indicate Exp 1, green diamonds represent Exp 2, and blue squares denote Exp 3.

2. Section 2: Theory and definitions

Fractures are mechanical discontinuities in rocks that consist of two rough surfaces in partial contact. Subsurface rocks are subjected to stresses arising from gravity, tectonic activity, uplift, and folding, commonly resulting in a multi-scale fracture network [2]. The gap between the two fractured surfaces, referred to as the "aperture", provides a path for fluid flow and transport, which is typically complex and heterogeneous. Fluid flow within a single fracture is given by a simplified reduced form of Navier-Stokes equation as described by cubic law, as given by Equation 3.

$$Q = -\frac{D<b>^3}{12\mu}\frac{dP}{L} \tag{1}$$

where, Q is the volumetric flow rate, D is diameter of sample, $<b>$ is fracture aperture, μ is viscosity of fluid, dP is pressure drop in the flow direction and L is the fracture length over which pressure drops takes place [3, 4, 5]. Comparing this with Darcy-like linear behavior for single-phase flow, $Q = -kA(dP/dx)$, the fracture permeability can be defined by equation 4.

$$k_f = \frac{<b>^2}{12} \tag{2}$$

However, in the case of two-phase flow, the effective permeability cannot be described by simple equations due to phase interference. It depends on the saturation fraction of each phase within the fracture. This permeability is typically expressed as relative permeability, which is strongly influenced by invasion displacement patterns. These patterns can range from capillary fingering to viscous fingering, depending on the fluid properties and fracture

characteristics. Fracture properties, such as mean aperture size and surface roughness, play a critical role in determining flow behavior. Natural fractures often exhibit highly rough surfaces and variable aperture distributions, further complicating the displacement dynamics. Fracture roughness can be quantified using various approaches [6, 7, 8]. For two-phase flow, an empirical parameter, the relative roughness index, λ_b is often used to assess the impact of roughness. It is defined as $\frac{<b>^\sigma}{<b>_m}$, where $< b >_m$ represents the mean aperture, and $< b >^\sigma$ is the standard deviation of the aperture [9, 10, 11, 12, 13]. The relative roughness index values for these samples are 0.72, 0.65, and 0.95, respectively.

3. Section 3: Experimental detailed procedure

The detailed procedure for the experiments is described as follows:

1. The sample was vacuum-dried overnight, wrapped with Teflon tape and aluminum foil to prevent gas leakage, placed inside a Viton sleeve, and subsequently loaded into the core holder.

2. A confining pressure of 1.5 MPa was applied to the sample using deionized water and the Reaxus pump, after which the core holder was mounted vertically on the stage of the X-ray CT scanner.

3. A dry scan was performed along the entire length of the sample.

4. The absolute permeability was determined by plotting q/A against $\Delta P/L$, with the slope corresponding to k/μ in Darcy's law. Fracture permeability was calculated using the local cubic law, shown in

equation 3. The fracture permeabilities of samples from Exp 1, 2 and 3 were 38 mD, 79 mD, and 298 mD, respectively.

$$Q = -\frac{D<b>^3}{12\mu}\frac{dP}{L} \tag{3}$$

where, Q is the volumetric flow rate, D is diameter of sample, $<b>$ is fracture aperture, μ is viscosity of fluid, dP is pressure drop in the flow direction and L is the fracture length over which pressure drops takes place [3, 4, 5]. Comparing this with Darcy-like linear behavior for single-phase flow, $Q = -k_f A(dP/dx)$, the fracture permeability can be defined by equation 4.

$$k_f = \frac{<b>^2}{12} \tag{4}$$

5. The water was displaced by non-H_2-equilibrated KI brine to achieve a fully brine-saturated fracture. The core was gradually heated to 65°C within one hour using heating tape wrapped around the core holder.

6. The flow system was pressurized with brine in 1 MPa increments, maintaining a 1.5-MPa difference between the confining and fracture pressures until reaching a fracture pressure of 10 MPa and a confining pressure of 11.5 MPa.

7. 10 mL of equilibrated brine from the reactor was pulled through the fractured sample using the ISCO pump, displacing the non-H_2-equilibrated brine from the fracture.

8. Equilibrated gas from the reactor was pulled through rock samples at the desired flow rate (as specified in Table 3 1). A high-quality scan was captured at the end of the drainage.

9. Equilibrated brine was re-injected to displace the gas and measure gas trapping. A high-quality scan was obtained at the end of the imbibition process.

For Exp 1 and 2 gas/brine are injected from the bottom injection port whereas for Exp 3 gas/brine are injected from the top of the sample.

4. Section 4: Fluid occupancy for large samples from Exp 2 and 3

The gas and brine distribution in the fracture a a function of distance. The distance is calculated as twice the maximum distance from the center of the aperture to the nearest wall of the fracture.

(a)

(b)

(c)
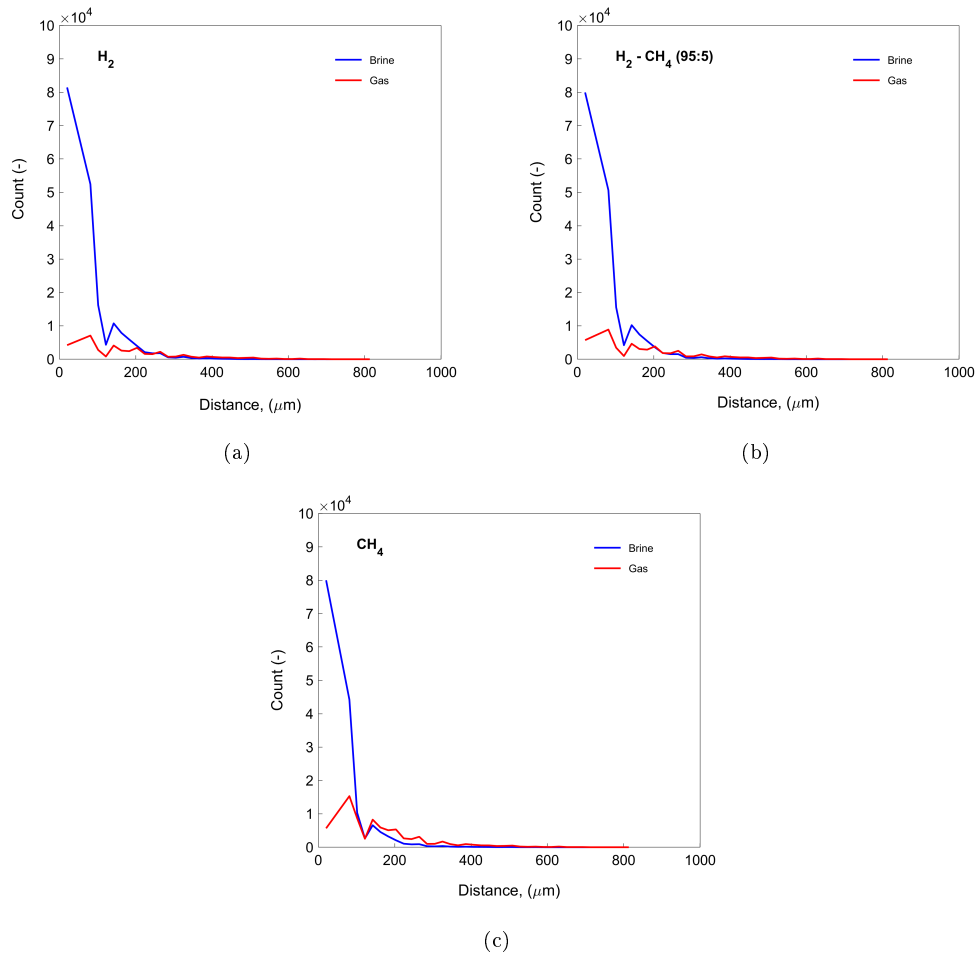
Figure S2: Fluid phase occupancy in Exp 2, D = 25 mm , $< b > = 255$ µm (a) H_2 (b) H_2 - CH_4 (5 : 95) (c) CH_4. The distance is calculated as twice the maximum distance from the center of the aperture to the nearest wall of the fracture.
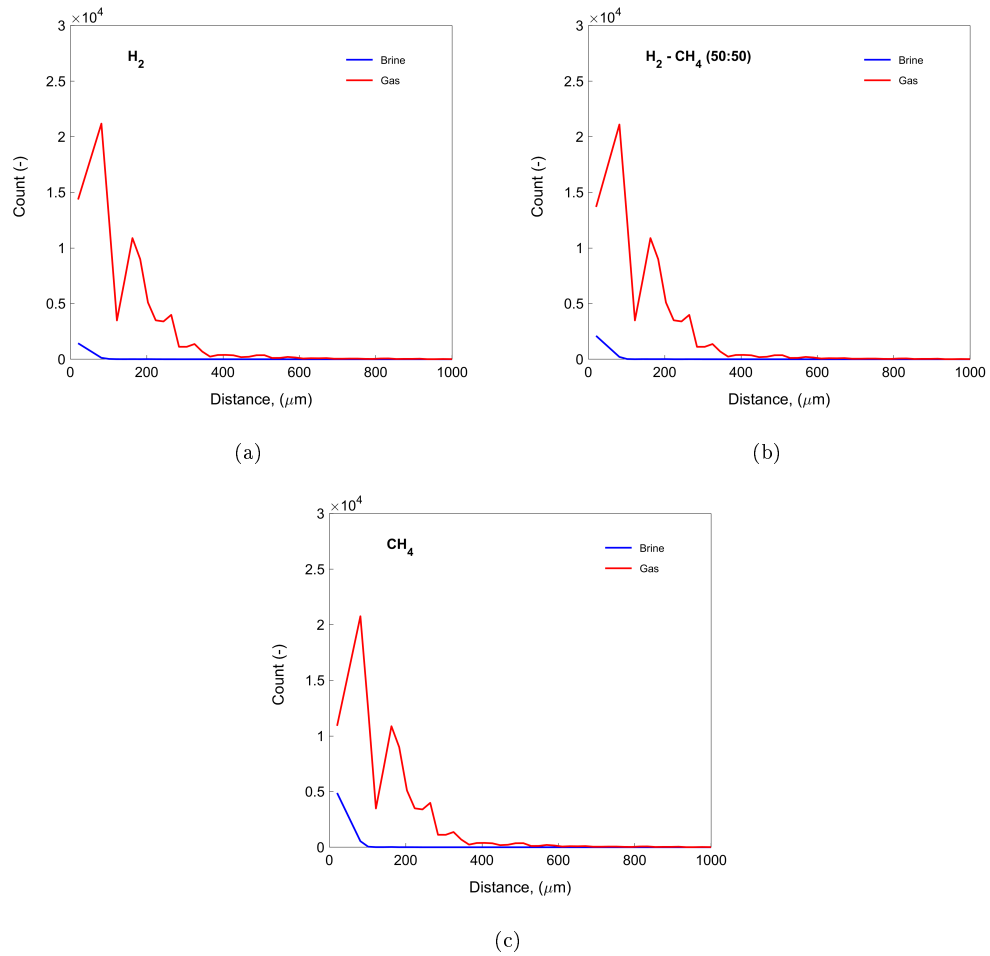
(a)

(b)

(c)

Figure S3: Fluid phase occupancy in Exp 3, D = 25 mm , $<b>$ = 450 μm (a) H_2 (b) H_2 - CH_4 (50 : 50) (c) CH_4. The distance is calculated as twice the maximum distance from the center of the aperture to the nearest wall of the fracture.

5. Section 5: Effect of aperture for CH_4 - brine distribution after drainage

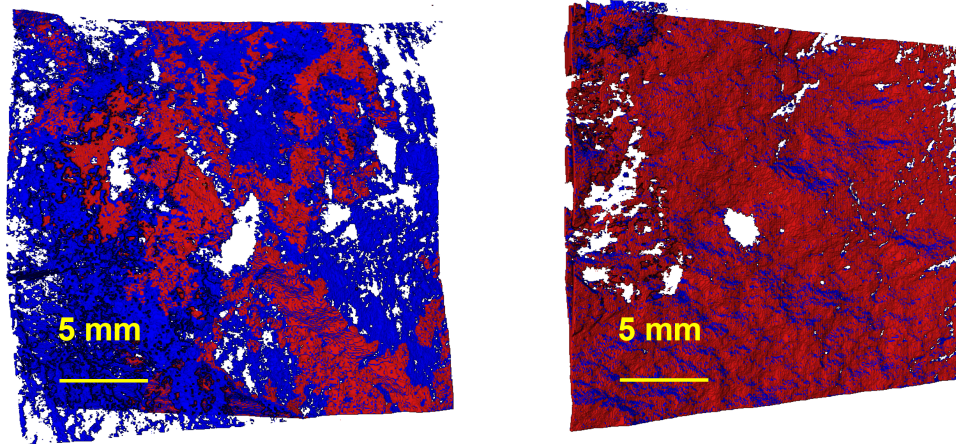CH_4 - brine distribution for Exp 2 and 3. The trend is similar to H_2 - brine distribution.

Figure S4: (3-D volume rendering of CH_4 - brine distribution after drainage (a) Exp 2: $< b > = 255$ µm. (b) Exp 3: $< b > = 450$ µm. The red color denotes gas and blue color denotes brine phase.

6. Section 6: Saturation for Exp 3 after imbibition

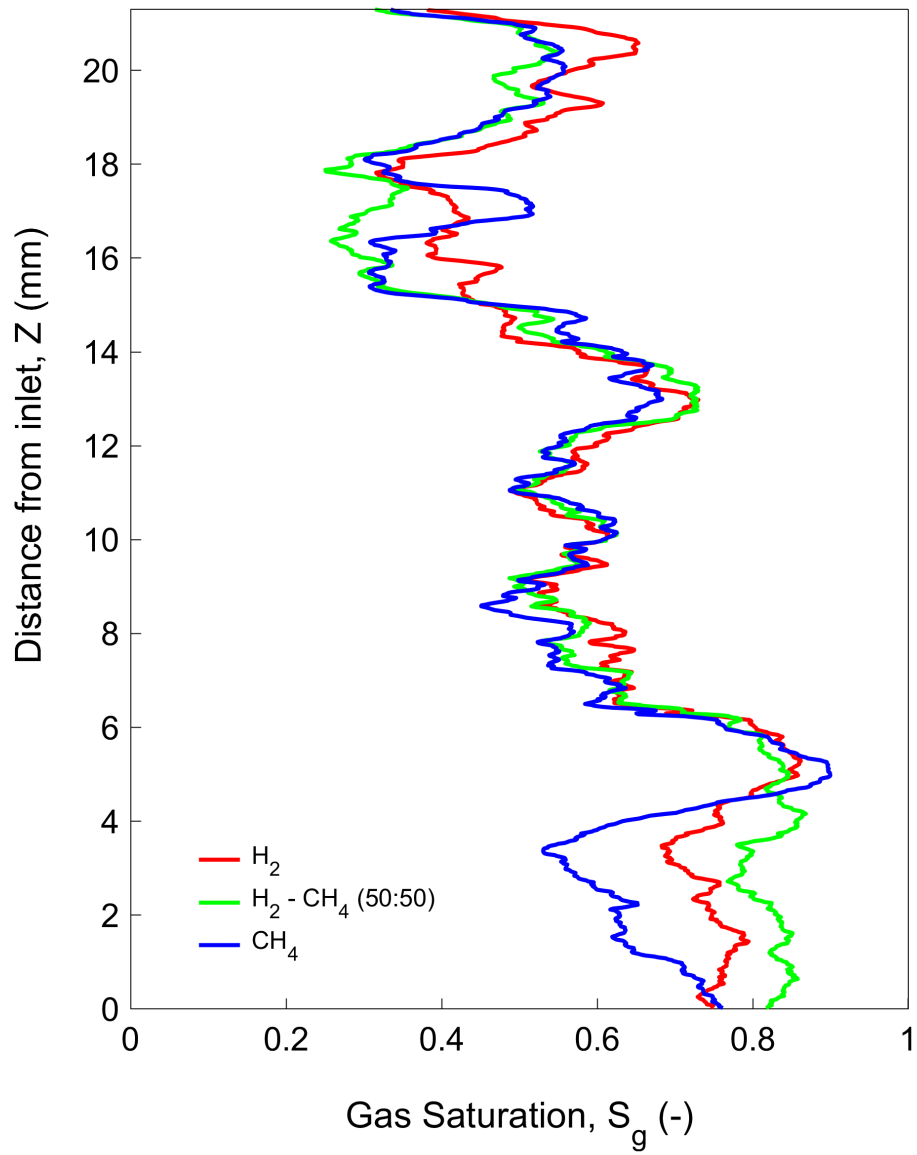1-D slice averaged gas saturation after imbibition for Exp 3.

Figure S5: 1-D slice-averaged of gas saturation after imbibition for Exp 3 : $<b> = 450$ μm.

7. Section 7: Disconnected gas ganglia after imbition in Exp 3

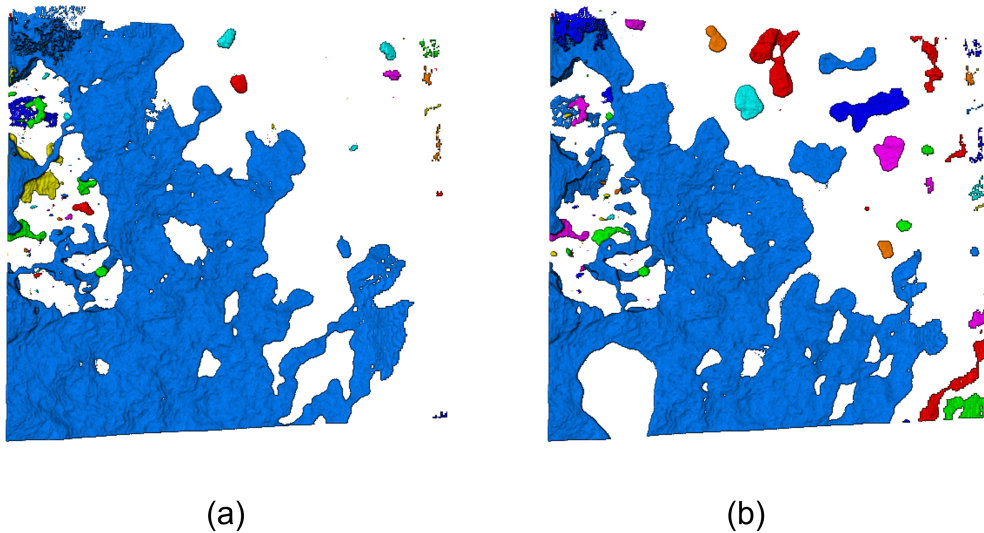Disconnected ganglia of gas after imbibition in Exp 3 with $<b> = 450$ µm.

(a)   (b)

Figure S6: 3-D volume rendering of gas after imbibition for Exp 3: $<b> = 450$ µm. (a) H_2 (b) CH_4. Each color represents a connected gas ganglia.

References

[1] Roland Lenormand, Eric Touboul, and Cesar Zarcone. Numerical models and experiments on immiscible displacements in porous media. *Journal of Fluid Mechanics*, 189(November):165–187, 1988. ISSN 14697645. doi: 10.1017/S0022112088000953.

[2] Robert W Zimmerman and Adriana Paluszny. *Fluid Flow in Fractured Rocks*. Wiley, 2003. ISBN 978-119-24802-6.

[3] Robert W. Zimmerman and Gudmundur S. Bodvarsson. Hydraulic conductivity of rock fractures. *Transport in Porous Media*, 23(1):1–30, 1996. ISSN 01693913. doi: 10.1007/BF00145263.

[4] D D Schrauf, TEvans. Laboratory Studies of Gas Flow Through a Single Natural Fracture. 22(7):1038–1050, 1986.

[5] Z. Chen, S.P. Narayan, Z. Yang, and S.S. Rahman. An experimental investigation of hydraulic behaviour of fractures and joints in granitic rock. *International Journal of Rock Mechanics and Mining Sciences*, 37(7): 1061–1071, 2000. doi: https://doi.org/10.1016/S1365-1609(00)00039-3.

[6] Nick Barton and Vishnu Choubey. The shear strength of rock joints in theory and practice. *Rock mechanics*, 10:1–54, 1977. doi: https://doi.org/10.1007/BF01261801.

[7] Nick Barton, SC Bandis, and K Bakhtar. Strength, deformation and conductivity coupling of rock joints. *International Journal of Rock Mechanics and Mining Sciences*, 22(3):121–140, 1985. doi: https://doi.org/10.1016/0148-9062(85)93227-9.

[8] R Olsson and N Barton. An improved model for hydromechanical coupling during shearing of rock joints. *International journal of rock mechanics and mining sciences*, 38(3):317–329, 2001. doi: https://doi.org/10.1016/S1365-1609(00)00079-4.

[9] Nick Barton and Eda F De Quadros. Joint aperture and roughness in the prediction of flow and groutability of rock masses. *nternational*

Journal of Rock Mechanics and Mining Sciences, 3-4(252-e1), 1997. doi: https://doi.org/10.1016/S1365-1609(97)00081-6.

[10] Ran Hu, Chen Xing Zhou, Dong Sheng Wu, Zhibing Yang, and Yi Feng Chen. Roughness Control on Multiphase Flow in Rock Fractures. *Geophysical Research Letters*, 46(21):12002–12011, 2019. ISSN 19448007. doi: 10.1029/2019GL084762.

[11] Lichun Wang and M. Bayani Cardenas. Transition from non-Fickian to Fickian longitudinal transport through 3-D rough fractures: Scale-(in)sensitivity and roughness dependence. *Journal of Contaminant Hydrology*, 198:1–10, 2017. doi: http://dx.doi.org/10.1016/j.jconhyd.2017.02.002.

[12] Zuyang Ye, Hui Hai Liu, Qinghui Jiang, and Chuangbing Zhou. Two-phase flow properties of a horizontal fracture: The effect of aperture distribution. *Advances in Water Resources*, 76:43–54, 2015. doi: http://dx.doi.org/10.1016/j.advwatres.2014.12.001.

[13] Tomos Phillips, Tom Bultreys, Jeroen van Stappen, Kamaljit Singh, Erik Clemens Boersheim, Sahyuo Achuo Dze, Stefanie von Offenwert, Ben Callow, Mostafa Borji, Vladimir Novak, Christian M. Schlepütz, Veerle Cnudde, Florian Doster, and Andreas Busch. Influence of Local Aperture Heterogeneity on Invading Fluid Connectivity During Rough Fracture Drainage. *SSRN Electronic Journal*, 151:2387–2403, 2023. doi: https://doi.org/10.1007/s11242-024-02117-5.